

國立臺灣大學理學院物理學系

碩士論文

Department of Physics

College of Science

National Taiwan University

Master Thesis



純量場暗物質暈的固有函數展開

Eigenfunction expansion for scalar field dark matter halos

林善長

Shan-Chang Lin

指導教授：闕志鴻 博士

Advisor: Tzihong Chiueh, Ph.D.

中華民國 105 年 7 月

July 2016

摘要

我們用固有函數展開分析了純量場暗物質暈的模擬。純量場暗物質符合泊松-薛丁格方程式，在宇宙晚期，當暗物質暈達成均功條件時，我們可以解不隨時間變的薛丁格方程式，並且得到固有函數跟相對應的機率振幅，我們發現機率分布函數的形式可以被古典無碰撞且會被自身重力影響的系統的機率分布函數描述，另外，我們發展了一個可以解出自洽的密度與重力位勢符的方法，這些解符合泊松-薛丁格方程式並且是平衡態，他的機率分布函數符合費米金模型。我們也使用模擬測試以自洽重力位勢造出來的暗物質暈的穩定性。

關鍵詞：暗物質暈、純量場暗物質、分布函數、宇宙學、泊松-薛丁格方程式

Eigenfunction expansion for scalar field dark matter halos



Shan-Chang Lin

Abstract

We analyze the simulation result of non-interacting scalar field dark matter halos using energy eigenfunction expansion. The scalar field dark matter obeys the Poisson-Schrodinger (SP) equation. At late time, when the dark matter halos are virialized, we can solve time independent Schrodinger equation and obtain amplitude of each eigenmode. We find that the distribution function (DF) of the dark matter halos can be described by models of classical distribution functions, and we develop a method to solve potential and density of a spherically symmetric Schrödinger-Poisson system whose distribution function obeys fermionic King model. Also, we construct artificial dark matter halos using different potentials, and test their stability. The amplitudes of the artificial halos are generated by fermionic King model.

Keywords

Scalar field dark matter, dark matter halo, probability distribution function, Schrödinger-Poisson equation



Contents

Contents	i
List of Figures	iii
1 Introduction	1
2 Equations and methods	3
2.1 The Schrödinger-Poisson equation	3
2.2 Distribution function	5
2.3 Procedure of solving eigenfunctions and amplitudes	7
2.4 Models of distribution function for classical collisionless self-gravitating system	10
2.4.1 Distribution function depends on energy	11
2.4.2 Distribution function depends on energy and L^2	12
2.5 Solving self-consistent solutions of fermionic King model	13
2.6 Method of constructing artificial halos	16
2.7 Time correlation function	17
3 Results	19
3.1 Probability distribution function	19
3.2 Self-consistent solution of fermionic King model	23
3.3 Artificial halos	26
3.4 Time correlation function	28
4 Conclusion	45

Bibliography





List of Figures

2.1	Density slice of ψ DM halo	18
3.1	Fitting models with energy distribution function, the error bar represent standard error.	20
3.2	Fitting models with energy distribution function	23
3.3	Fitting models with energy distribution function, we exclude nine highest bins for this case	24
3.4	Fitting models with energy distribution function, we exclude nine highest bins for this case	25
3.5	Fitting models with energy distribution function. We exclude nine highest bins for this case	26
3.6	OM King model Run03 Halo01_06 time072	27
3.7	OM King model Run03 Halo05 time072	28
3.8	29
3.9	(a)density profile of self-consistent solution(green) and simulation halo(blue). (b)input(red) and output(green) potential of fifth iteration compare with simulation halo(blue)	30
3.10	(a)density profile of self-consistent solution(green) and simulation halo(blue). (b)input(red) and output(green) potential of fifth iteration compare with simulation halo(blue)	31
3.11	(a)density profile of self-consistent solution(green) and simulation halo(blue). (b)input(red) and output(green) potential of fifth iteration compare with simulation halo(blue)	32

3.12 (a)density profile of self-consistent solution(green) and simulation halo(blue). (b)input(red) and output(green) potential of fifth iteration compare with simulation halo(blue)	33
3.13 (a)density profile of self-consistent solution(green) and simulation halo(blue). (b)input(red) and output(green) potential of fifth iteration compare with simulation halo(blue)	34
3.14 (a)density profile of self-consistent solution(green) and simulation halo(blue). (b)input(red) and output(green) potential of fifth iteration compare with simulation halo(blue)	35
3.15 (a)density profile of self-consistent solution with different β . (b)output potential of self-consistent solution with different β	36
3.16 (a)density profile of self-consistent solution with different μ . (b)output potential of self-consistent solution with different μ	37
3.17 Distribution function fitted by $\beta = 3.4$, $\mu = -2.5$, and $E_c = 0$ (red) compare with direct fitting(green).	38
3.18 Self-consistent solution with parameters obtained from fitting(a)density profile of self-consistent solution(green) and simulation halo(blue). (b)input(red) and output(green) potential of fifth iteration compare with simulation halo(blue).	39
3.19 Density slice of ψ DM halo	40
3.20 Density slice of ψ DM halo	41
3.21 Density profile evolves about one free-fall time at virial radius. Here the red curve denote artificial halo construct by simulation potential, and blue curves denote simulation halo. Soliton oscillate in both cases and the outer part of halos are stable as well.	42

- 3.22 Density profile evolves about one free-fall time at virial radius. The Arti-Old denote the artificial halo constructed by soliton plus NFW potential. Arti-New denote artificial halo constructed by self-consistent solution potential with $\beta = 3.4$ and $\mu = -2.5$. The self-consistent solution halo is stable while with soliton oscillate slightly compare to simulation halo. While soliton plus NFW halo need time to relax to a steady state. 43
- 3.23 Time correlation function of self-consistent solution with $\beta = 3.4$ and $\mu = -2.5$ 44



Chapter 1

Introduction

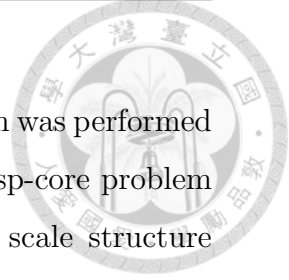
During last decade, several small scale tensions between standard cold dark matter(CDM) and observations have received much attention, including cusp-core problem and missing satellites problem [1]. Simulations of CDM structure formation found cusp-like density profile in the inner part of halos [2, 3], while observation found that density profile of the inner region of dwarf galaxies seem to have flat cores [4–7]. On the other hand, the predicted amount of subhalos by CDM [8] are much less than the amount of satellite galaxies detected in the Local Group [9]. While this issue may be caused by the limitation of survey methods or the limitation of sensitivity of observational tools, we could consider this problem to be a sign of discrepancy between CDM model and observations.

The scalar field dark matter(SFDM) was proposed to solve the small scale problems mentioned above. It can be divided into two categories, with [10,11] or without self-interaction [12,13]. Among these SFDM model, we are more interested in scalar field without self-interaction, which is also called fuzzy cold dark matter(FCDM) or ψ dark matter(ψDM). ψDM particles are extremely light non-relativistic boson whose masses are around 10^{-22} eV. The mass of ψDM particle is light enough that the critical temperature of forming Bose-Einstein condensation(BEC) is high enough to approximate all dark matter particles to be in the BEC state, therefore it can be described by a single particle wave function under Newtonian approximation. The uncertainty principle helps ψDM model avoid the formation of halo cusps as well as suppress the abundance of subhalos. Moreover, ψDM behaves like CDM on large

scale, in which the predictions of CDM agree with observations .

In 2014, first cosmological simulation of ψDM structure formation was performed by Schive et al [14], showing that ψDM model indeed solve the cusp-core problem and missing satellite problem simultaneously, while leaving large scale structure similar to cold dark matter simulation. Base on this work, they found that dark matter halos are composed of a solitonic core surrounded by a extended halo with various granule-like structure. The size of these granules are about several kpc. Note that the density profile in the simulation is different from the analytical solution [15] and the self-interaction case in Thomas-Fermi approximation [11].

We analyzed dark matter halos in our simulation by eigenfunction expansion, assuming dark matter halos are spherical-symmetric systems. We find the probability distribution function, which is defined in section 2.2, can be fitted by several classical distribution function models which describe self-gravitating collisionless systems [16]. Moreover, we constructed an artificial halos based on our analysis of distribution function, and test its stability by simulation. On the other hand, if we take the distribution function to be the fermionic King model [17], which would be discuss in section 2.3, we can obtain a series of self-consistent solutions of halo potential. This method is described in section 2.4. Besides, we calculated the time correlation function to study the dynamical properties of the granules in dark matter halos, using the artificial halo we constructed. The results are shown in section 3.4.





Chapter 2

Equations and methods

2.1 The Schrödinger-Poisson equation

In this section we briefly derive the equation of motion for ψDM . In the non-relativistic limit, the Einstein-Klein-Gordon (EKG) equation reduce to Schrödinger-Poisson (SP) equation [18]. The derivation follows the content in [19].

The ψDM is described by the Klein-Gordon equation

$$\square\phi + \frac{m^2 c^2}{\hbar^2}\phi = 0 \quad (2.1)$$

where

$$\square = D_\mu(g^{\mu\nu}\partial_\nu) = \frac{1}{\sqrt{-g}}\partial_\mu(\sqrt{-g}g^{\mu\nu}\partial_\nu) \quad (2.2)$$

is the d'Alembertian operator.

In the weak field limit $\Phi/c^2 \ll 1$, the Friedmann-Robertson-Walker(FRW) metric with scalar perturbation in conformal Newtonian gauge is

$$ds^2 = g_{\mu\nu}dx^\mu dx^\nu = c^2(1 + 2\frac{\Phi}{c^2})dt^2 - a(t)(1 - 2\frac{\Phi}{c^2})\delta_{ij}dx^i dx^j \quad (2.3)$$

where $a(t)$ is the scale factor, and $\Phi(\vec{x}, t)$ is the gravitational potential of Newtonian gravity. Substituting equation 2.3 into equation 2.1, we have the Klein-Gordon equation

$$\frac{1}{c^2}\frac{\partial^2\phi}{\partial t^2} + \frac{3H}{c^2}\frac{\partial\phi}{\partial t} - \frac{1}{a^2}(1 + \frac{4\Phi}{c^2})\nabla^2\phi - \frac{4}{c^4}\frac{\partial\Phi}{\partial t}\frac{\partial\phi}{\partial t} + (1 + \frac{2\Phi}{c^2})\frac{m^2 c^2}{\hbar^2}\phi = 0 \quad (2.4)$$

up to first order of Φ/c^2 , where $H = \dot{a}/a$ is the Hubble constant.

We also have Einstein equation

$$R_{\mu\nu} - \frac{1}{2}g_{\mu\nu}R = \frac{8\pi G}{c^4}T_{\mu\nu} \quad (2.5)$$

Assuming ψDM dominate the energy density of the Universe, one can obtain

$$\frac{\nabla^2\Phi}{4\pi Ga^2} = \frac{T_0^0}{c^2} - \frac{3H^2}{8\pi G} + \frac{3H}{4\pi Gc^2}\left(\frac{\partial\Phi}{\partial t} + H\Phi\right) \quad (2.6)$$

with Newtonian gauge for the time-time component of Einstein equation.

$$R_0^0 - \frac{1}{2}R = \frac{8\pi G}{c^4}T_0^0 \quad (2.7)$$

In the non-relativistic limit, we take the transformation [20]

$$\phi(x, t) = \frac{\hbar}{m}e^{-imc^2t/\hbar}\psi(x, t) \quad (2.8)$$

Here ψ can be interpreted as wave function only in the non-relativistic limit $c \rightarrow \infty$, and so does $\rho = |\psi|^2$ which is rest mass density when $c \rightarrow \infty$. Substitute equation (2.8) into Klein-Gordon equation (2.4) and Einstein equation (2.6), we have

$$\begin{aligned} i\hbar\frac{\partial\psi}{\partial t} - \frac{\hbar^2}{2mc^2}\frac{\partial^2\psi}{\partial t^2} - \frac{3}{2}H\frac{\hbar^2}{mc^2}\frac{\partial\psi}{\partial t} + \frac{\hbar^2}{2ma^2}\left(1 + \frac{4\Phi}{c^2}\right)\nabla^2\psi \\ - m\Phi\psi + \frac{3}{2}i\hbar H\psi + \frac{2\hbar^2}{mc^4}\frac{\partial\Phi}{\partial t}\left(\frac{\partial\psi}{\partial t} - \frac{imc^2}{\hbar}\psi\right) = 0 \end{aligned} \quad (2.9)$$

and

$$\begin{aligned} \frac{\nabla^2\Phi}{4\pi Ga^2} = \left(1 - \frac{\Phi}{c^2}\right)|\psi|^2 + \frac{\hbar^2}{2m^2c^4}\left(1 - \frac{2\Phi}{c^2}\right)\left|\frac{\partial\psi}{\partial t}\right|^2 + \frac{\hbar^2}{2a^2m^2c^2}\left(1 + \frac{2\Phi}{c^2}\right)|\nabla\psi|^2 \\ - \frac{\hbar}{mc^2}\left(1 - \frac{2\Phi}{c^2}\right)Im\left(\frac{\partial\psi}{\partial t}\psi^*\right) - \frac{3H^2}{8\pi G} + \frac{3H}{4\pi Gc^2}\left(\frac{\partial\Phi}{\partial t} + H\Phi\right) \end{aligned} \quad (2.10)$$

In the non-relativistic limit $c \rightarrow \infty$, equation (2.9) and (2.10) reduce to Schrödinger-Poisson equation

$$i\hbar\frac{\partial\psi}{\partial t} + \frac{3}{2}i\hbar H\psi = -\frac{\hbar^2}{2ma^2}\nabla^2\psi + m\Phi\psi \quad (2.11)$$

and

$$\frac{\nabla^2\Phi}{4\pi Ga^2} = |\psi|^2 - \frac{3H^2}{8\pi G} \quad (2.12)$$

For the homogeneous background wave function $\psi_b(x, t) = \psi_b(t)$ and $\Phi_b(x, t) = 0$, equation (2.11) and (2.12) become

$$i\hbar\frac{\partial\psi_b}{\partial t} = -\frac{3}{2}i\hbar H\psi_b \quad (2.13)$$



and

$$|\psi_b|^2 = \frac{3H^2}{8\pi G} \quad (2.14)$$

Therefore,

$$\psi_b \propto a^{-3/2} \quad (2.15)$$

and the density

$$\rho_b = |\psi_b|^2 \propto a^{-3} \quad (2.16)$$

scales as matter.

We write Schrödinger-Poisson equation into dimensionless equation and assume the time scale of evolution is much faster than cosmological expansion. Therefore, the second term of equation (2.11) on the left hand side can be ignored. We have

$$i\hbar \frac{\partial \psi}{\partial t} = -\frac{\hbar^2}{2ma^2} \nabla^2 \psi + m\Phi \psi \quad (2.17)$$

and

$$\frac{\nabla^2 \Phi}{4\pi G a^2} = |\psi|^2 - \frac{3H^2}{8\pi G} \quad (2.18)$$

normalize these equation with normalized length $\vec{\xi} \equiv (\frac{3}{2}H_0^2\Omega_{m0})^{-1/4}(m_B/\hbar)^{1/2}$, normalized time coordinate $\tau \equiv (\frac{3}{2}H_0^2\Omega_{m0})^{1/2}a^{-2}t$, normalized comoving density $|\psi|^2 = \rho/\rho_b$ and normalized potential $V = m_B a \hbar^{-1} (\frac{3}{2}H_0^2\Omega_{m0})^{-1/2}\Phi$, we obtain

$$i \frac{\partial \psi}{\partial \tau} = \left(-\frac{\nabla^2}{2} + aV\right)\psi \quad (2.19)$$

and

$$\nabla^2 V = |\psi|^2 - 1 \quad (2.20)$$

, which is the Schrödinger-Poisson equation.

2.2 Distribution function

From the von Neumann equation

$$i\hbar \frac{\partial \rho}{\partial t} = [H, \rho] \quad (2.21)$$

, where ρ is density operator and H is the Hamiltonian of this system, we know that if the given system is in a equilibrium state, that is, $\frac{\partial \rho}{\partial t} = 0$, the density operator



has to be an explicit function of Hamiltonian in order to make the right hand side of equation (2.21) vanish. Moreover, we assume the system is spherical-symmetric and adopt the treatment of standard quantum mechanics. It means that we have a set of basis $|nlm\rangle$ which are the eigenkets of Hamiltonian(H), angular momentum square(L^2), and z-component of angular momentum(L_z), and they satisfy

$$H|nlm\rangle = E_{nl}|nlm\rangle \quad (2.22)$$

$$L^2|nlm\rangle = \hbar^2 l(l+1)|nlm\rangle \quad (2.23)$$

$$L_z|nlm\rangle = \hbar m|nlm\rangle \quad (2.24)$$

We consider an ensemble of N identical systems described by the Schrödinger-Poisson equation. Let $\psi^k(r, t)$ denote the wave function of the k th system at time t . It follows the Schrödinger-Poisson equation

$$i\frac{\partial\psi^k}{\partial\tau} = \left(-\frac{\nabla^2}{2} + aV\right)\psi^k \quad (2.25)$$

and

$$\nabla^2 V = |\psi^k|^2 - 1 \quad (2.26)$$

We introduce the complete orthonormal eigenfunctions

$$\Phi_{nlm} = \langle x|nlm\rangle \quad (2.27)$$

, and the wavefunction can be expanded by this set of functions

$$\psi(r, \tau) = \sum_{nlm} a_{nlm}(\tau)\Phi_{nlm}(r) \quad (2.28)$$

, where a_{nlm} is the probability amplitudes for a system to be in the states Φ_{nlm} . The density operator $\hat{\rho}$ is defined by the matrix elements as

$$\rho_{nlmn'l'm'} = \frac{1}{N} \sum_{k=1}^N a_{nlm}^k a_{n'l'm'}^{k*} \quad (2.29)$$

The off-diagonal elements vanish because of the postulate of random phases. We define the distribution function to be the diagonal elements of density operator expanded by the complete orthonormal set $\Phi_{nlm}(r)$

$$\rho_{nlmn'l'm'} = f(E_{nl}, l, m)\delta_{nn'}\delta_{ll'}\delta_{mm'} \quad (2.30)$$

The physical meaning of the distribution function defined in this way is the probability of finding the system to be in the state Φ_{nlm} .

As we mentioned above, the distribution function may depend on energy eigenvalues (E_{nl}), angular momentum square (L^2), and the z-component of angular momentum. Note that this is similar to the result of Jeans theorem, which states that any solution of steady state of collisionless Boltzmann equation depends only on the integrals of motion. And for a spherical symmetric system the integrals of motion is Hamiltonian, and angular momentum.

Practically, we do not have ensembles which have the same halo mass in our simulations, thus we adopt the idea that the ensemble average of the amplitude squares will be the average of the amplitude squares over those states which have approximately the same eigenvalues. For example, if the distribution function only depends on energy eigenvalues, the distribution function will be computed by

$$f(E) = \frac{\sum_{E_{nl} \approx E} |a_{nlm}|^2}{g(E)} \quad (2.31)$$

where $g(E)$ is the density of states, that is, the number of states whose energy eigenvalues are in the neighborhood of energy E .

If the distribution function depends on both energy and L^2

$$f = f(E, L^2) \quad (2.32)$$

, then the distribution function will be

$$f(E, L^2) = \frac{\sum_{E_{nl} \approx E, l(l+1) \approx L^2} |a_{nlm}|^2}{g(E, L^2)} \quad (2.33)$$

where $g(E, L^2)$ again represents the density of states near E and L^2 .

2.3 Procedure of solving eigenfunctions and amplitudes

In this section, we introduce our method of solving radial eigenfunction by computer program, and some details we should notice when adopt this procedure.

First, we have spatial information of wave function $\psi(x, t)$ in a three dimensional simulation box at a certain time(usually at red shift zero). We only analyze the region inside the virial radius of halos. We adopt the definition that virial radius is the radius whose enclosed average density is 347 times background matter density[].

Next, we calculate the density profile of halos, while let density outside virial radius be zero. We extend our calculation domain of eigenfunction to about ten times of the virial radius, and compute gravitational potential by Green function method.

$$V(r) = -G \int \frac{\rho(r')}{|\vec{r}' - \vec{r}|} r'^2 \sin \theta d\theta d\phi dr' \quad (2.34)$$

where G is the Newton constant. Note that equation (2.34) implies

$$\lim_{r \rightarrow \infty} V(r) = 0 \quad (2.35)$$

because we neglect the boundary term. Also, because we set density outside the virial radius be zero, the potential outside the virial radius is

$$V(r) = -\frac{GM_{vir}}{r} \quad \text{for } r > r_{vir} \quad (2.36)$$

, where M_{vir} is the mass enclosed by virial radius.

Next, we solve the eigenfunction of hamiltonian operator

$$H = -\frac{\nabla^2}{2} + aV \quad (2.37)$$

, using separation of variable and standard treatment of spherical system in quantum mechanics textbook. We have

$$\psi(r, \theta, \phi) = R(r)Y_l^m(\theta, \phi) \quad (2.38)$$

where $Y_l^m(\theta, \phi)$ is the spherical harmonics, which satisfies

$$\sin \theta \frac{\partial}{\partial \theta} \left(\sin \theta \frac{\partial Y_l^m}{\partial \theta} \right) + \frac{\partial^2 Y_l^m}{\partial \phi^2} = -l(l+1) \sin^2 \theta Y_l^m \quad (2.39)$$

and $R(r) = u(r)/r$ is the radial wave function, where $u(r)$ satisfies

$$-\frac{1}{2} \frac{d^2 u}{dr^2} + \left(aV(r) + \frac{l(l+1)}{2r^2} \right) u = Eu \quad (2.40)$$

We use the package LAPACK [21] to calculate equation (2.40), and use finite difference method, that is,

$$-\frac{1}{2} \frac{1}{(\Delta r)^2} (u_{i+2} - 2u_{i+1} + u_i) + V_{\text{eff}} u_{i+1} = E u_{i+1} \quad (2.41)$$

where $V_{\text{eff}} = aV(r) + \frac{l(l+1)}{2r^2}$ is the effective potential. Finally, we normalize the solution such that

$$\int_0^{r_m} |R|^2 r^2 dr = 1 \quad (2.42)$$

where r_m is the maximum radius of our calculation domain.

For some quantum number l , we could obtain many eigenfunctions with different eigenvalue. Label these eigenfunctions from the lowest eigenvalue to the highest, we have another quantum number. Thus the eigenfunctions can be label by three quantum number n , l , and m ,

$$\Phi_{nlm}(r, \theta, \phi) = R_{nl}(r) Y_l^m(\theta, \phi) \quad (2.43)$$

which is analogous to the hydrogen atom.

Note that we set the upper limit of eigenvalues to be $-GM_{\text{vir}} m_B / r_{\text{vir}}$ when solving equation (2.41) for two reasons. First, the potential outside the virial radius is not correct because we artificially set the density outside be zero. Second, we can not let the upper limit of eigenvalues be zero because our radius domain is finite. There is a constraint of upper limit of eigenvalues for radial equation (2.40) in finite domain, see reference [22].

By using the orthogonality of eigenfunctions,

$$\int \Phi_{nlm}(r, \theta, \phi) \Phi_{n'l'm'}^*(r, \theta, \phi) d^3 r = \delta_{nn'} \delta_{ll'} \delta_{mm'} \quad (2.44)$$

we can solve the amplitudes of each eigenfunction.

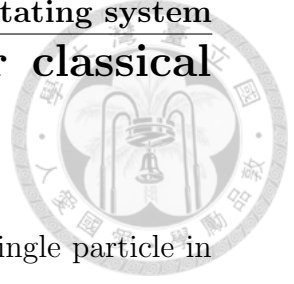
$$\psi(r, \theta, \phi) = \sum_{nlm} a_{nlm} \Phi_{nlm}(r, \theta, \phi) \quad (2.45)$$

where

$$a_{nlm} = \int \psi(r, \theta, \phi) \Phi_{nlm}^*(r, \theta, \phi) d^3 r \quad (2.46)$$

After we have the information of amplitudes, we can compute distribution function in terms of section 2.2.

2.4 Models of distribution function for classical collisionless self-gravitating system



In classical kinetic theory, we can define distribution function for single particle in the phase space

$$f = f(\vec{x}, \vec{v}, t) \tag{2.47}$$

such that $f(\vec{x}, \vec{v}, t)d^3x d^3v$ is the probability of finding the particle near the position \vec{x} and velocity \vec{v} at time t . The equation govern the distribution function is the Boltzmann transfer equation

$$\frac{\partial f}{\partial t} + \dot{\vec{x}} \cdot \frac{\partial f}{\partial \vec{x}} + \dot{\vec{v}} \cdot \frac{\partial f}{\partial \vec{v}} = \left(\frac{\partial f}{\partial t} \right)_{\text{coll}} \tag{2.48}$$

where the right hand side of equation (2.48) is due to collision with other particles. If the particle is collisionless, we have

$$\frac{\partial f}{\partial t} + \dot{\vec{x}} \cdot \frac{\partial f}{\partial \vec{x}} + \dot{\vec{v}} \cdot \frac{\partial f}{\partial \vec{v}} = 0 \tag{2.49}$$

for system with gravitation potential $\Phi(\vec{x}, t)$, equation (2.49) becomes

$$\frac{\partial f}{\partial t} + \dot{\vec{x}} \cdot \frac{\partial f}{\partial \vec{x}} - \frac{\partial \Phi}{\partial \vec{x}} \cdot \frac{\partial f}{\partial \vec{v}} = 0 \tag{2.50}$$

, which is called collisionless Boltzmann equation. For classical collisionless system with self gravity, there is no distribution function can maximize entropy of a system with energy E and total mass M . Accordingly, those system can only reach dynamical equilibrium rather than thermal equilibrium, and the distribution function will not be Maxwell-Boltzmann distribution. In fact, the distribution function of collisionless self-gravitating system is determined by initial condition and dynamical processes occurred [16].

Jeans theorem states that any steady-state solution of the collisionless Boltzmann equation depends on the phase-space coordinate only through integrals of motion in the given potential, and any function of the integrals yields a steady-state solution of the collisionless Boltzmann equation [16]. For a spherically symmetric system, Hamiltonian H and three components of angular momentum \vec{L} is the integrals of

motion. As a result, the distribution function of a spherically symmetric system depends on H and \vec{L} , that is,

$$f = f(H, \vec{L}) \quad (2.51)$$

There are several widely-used models of distribution function which satisfy the collisionless Boltzmann equation (2.50) and Poisson's equation

$$\nabla^2 \Phi = 4\pi G \rho \quad (2.52)$$

, where $\rho = \int f d^3v$.

2.4.1 Distribution function depends on energy

Now we consider distribution function only depends on the Hamiltonian H , $f = f(H)$. First, we introduce Hernquist model [23], which is written as

$$f_H(H) = \frac{1}{\sqrt{2}(2\pi)^3(GMa)^{3/2}} \frac{\sqrt{\tilde{\mathcal{E}}}}{(1 - \tilde{\mathcal{E}})^2} \left[(1 - 2\tilde{\mathcal{E}})(8\tilde{\mathcal{E}}^2 - 8\tilde{\mathcal{E}} - 3) + \frac{3 \sin^{-1} \sqrt{\tilde{\mathcal{E}}}}{\sqrt{\tilde{\mathcal{E}}(1 - \tilde{\mathcal{E}})}} \right] \quad (2.53)$$

, where a and M is parameters, G is gravitation constant and $\tilde{\mathcal{E}} \equiv -\frac{aH}{GM}$.

Another example is the Jaffe model [24], the distribution function of Jaffe model is

$$f_J(H) = \frac{1}{2\pi^3(GMa^{3/2})} \left[F_- \left(\sqrt{2\tilde{\mathcal{E}}} \right) - \sqrt{2}F_- \left(\sqrt{\tilde{\mathcal{E}}} \right) - \sqrt{2}F_+ \left(\sqrt{\tilde{\mathcal{E}}} \right) + F_+ \left(\sqrt{2\tilde{\mathcal{E}}} \right) \right] \quad (2.54)$$

where $F_{\pm}(z)$ is Dawson's integral defined as

$$F_{\pm}(z) = e^{\mp z^2} \int_0^z dy e^{\pm y^2} \quad (2.55)$$

The third one is Wilson's model [25], which is

$$f_W = \begin{cases} A [e^{-\beta(E-E_c)} - 1 + \beta(E - E_c)], & \text{if } E \leq E_c \\ 0, & \text{otherwise} \end{cases} \quad (2.56)$$

where E_c is the escape energy, which is the largest available energy of particles in this system, β and A are parameters. Note that the escape energy should be smaller than zero because we set the energy of a particle at rest at infinite to be zero.

Finally, we introduce King model [26] and fermionic King model. King model were first introduced by Michie [27] while were spread by King. The distribution function of King model is

$$f_{\text{King}} = \begin{cases} A(e^{-\beta(E-E_c)} - 1), & \text{if } E \leq E_c \\ 0, & \text{otherwise} \end{cases} \quad (2.57)$$

where E_c is again the escape energy. King model differ from Maxwell-Boltzmann distribution only by a constant, but this difference is important when we deal with self-gravitating system. King model describe a self-gravitating system with finite mass and finite radius, where the density drop to zero. While Maxwell-Boltzmann distribution result in infinite mass systems, whose density decrease as r^{-2} at large radius.

On the other hand, fermionic King model was introduced by Ruffini and Stella [28], and can be derived from kinetic theory [17]. The distribution function of fermionic King model reads

$$f_{\text{FK}} = \begin{cases} A \frac{e^{-\beta(E-E_c)} - 1}{e^{-\beta(E-E_c-\mu)} + 1}, & \text{if } E \leq E_c \\ 0, & \text{otherwise} \end{cases} \quad (2.58)$$

Fermionic King model may describe systems composed of fermion or systems which have experienced violent relaxation [29]. Violent relaxation happens when the potential of collisionless system depends on both space and time, and lead to a Fermi-Dirac type distribution function. However, Fermi-Dirac distribution function couple with gravity will result in infinite mass. Fermionic King model may provide a more realistic distribution function because it describe a finite mass system, while leaving particles with energy $E \ll E_c$ distribute as Fermi-Dirac distribution.

2.4.2 Distribution function depends on energy and L^2

Systems with distribution function of the form $f = f(H, L)$ are also spherically symmetric, but anisotropic in velocity distribution. That is,

$$\overline{v_r^2} \neq \overline{v_\theta^2} \quad (2.59)$$

Since the simulations of ψDM show anisotropic in derivatives at outer radius (see figure 2.1 for example), we expect that the distribution function may depend on angular momentum square L^2 .

First we introduce Osipkov-Merritt models [16], the distribution function depends on H and L only through the combination

$$Q \equiv -E - \frac{L^2}{2r_a^2}, \quad (2.60)$$

where r_a is a constant, called the anisotropy radius. By replacing the Hamiltonian with Q for distribution function mentioned in section 2.4.1, we obtain Osipkov-Merritt models.

Another model we want to consider is Michie model, which is an extension of King model to include anisotropy, defined by the distribution function

$$f_M = \begin{cases} Ae^{-\beta L^2/(2r_a^2)}(e^{-\beta(E-E_c)} - 1), & \text{if } E \leq E_c \\ 0, & \text{otherwise} \end{cases} \quad (2.61)$$

where A and β are parameters, In the limit $r_a \rightarrow \infty$ this distribution function reduce to King model (equation 2.57), and for $E - E_c \ll \sigma^2$

$$f \approx \rho_1 (2\pi\sigma^2)^{-3/2} e^{-L^2/(2r_a^2\sigma^2)} e^{-(E-E_c)/\sigma^2} = Ae^Q, \quad (2.62)$$

which is the Osipkov-Merritt models.

The distribution function of simulation halos as well as the results of fitting with models in this section are shown in section 3.1. Although the Schrödinger-Poisson system is quantum system, which can not be described by collisionless Boltzmann equation (equation 2.50), the distribution function can be fitted by those classical models fairly well.

2.5 Solving self-consistent solutions of fermionic King model

Our goal is to create spherically symmetric stable halos for given halo masses with some parameters for a certain distribution function. We apply the recipe describe

in this section for fermionic King model, and we will discuss how the parameters affect the density profile in section 3.2.

A self-consistent solution satisfies equations

$$-\frac{\hbar^2}{2ma^2}\nabla^2\Phi_{nlm} + m\Phi\Phi_{nlm} = E_{nl}\Phi_{nlm} \quad (2.63)$$

$$\psi = \sum_{nlm} a_{nlm}\Phi_{nlm} \quad (2.64)$$

$$\nabla^2\Phi = 4\pi Ga^2\rho = 4\pi Ga^2|\psi|^2 \quad (2.65)$$

$$\langle a_{nlm}a_{n'l'm'}^* \rangle_{en} = f_{FK}(E_{nl})\delta_{nn'}\delta_{ll'}\delta_{mm'} \quad (2.66)$$

, where $\langle \rangle_{en}$ denote the ensemble average, f_{FK} is the fermionic King model distribution function (equation 2.58), a is scale factor and a_{nlm} is amplitudes of eigenmodes. Note that here the density is dimensionless and normalized with background matter density, and we ignore -1 in Poisson's equation because density inside virial radius is roughly few hundreds of background density.

We will depict the main idea and describe details in the next few paragraphs. The idea is simple and straightforward. First, guess a initial potential Φ_{in} and solve the eigenvalues equation (2.63). Next, generate amplitude according to equation (2.66). Here we do not use random number to generate amplitudes, simply set all amplitudes $a_{nlm} = \sqrt{f_{FK}(E_{nl})}$. Third step is generating wave function and potential Φ_{out} by equation (2.64) and (2.65). As one may expect, the output potential Φ_{out} will not be the same with input potential Φ_{in} . Therefore, we adopt time independent perturbation theory, changing the energy E_{nl} to $E_{nl} + \Delta E_{nl}$, generating amplitudes again and obtaining another potential Φ_{per} . Then use the potential Φ_{per} to solve equation (2.63), and repeat these steps until the potential converge to a self-consistent solution, that is, $\Phi_{in} = \Phi_{out}$. We found that this procedure converge rapidly if the parameters of initial input potential is suitable and diverge otherwise. It will converge within ten iterations if we guess the right parameters of initial potential.

First we will briefly describe how to create initial potential. For a given halo mass, there is a core-halo relation found by simulation [30]. Thus we have soliton mass correspond to this halo mass and a core radius defined as the radius where density decrease to half of the central density. According to [14], soliton density

profile can be approximated by

$$\rho_s(r) \approx \frac{1.9(m_B/10^{-23}eV)^{-2}(r_c/kpc)^{-4}}{[1 + 9.1 \times 10^{-2}(r/r_c)^2]^8} \quad (2.67)$$

, where r_c is the core radius. On the other hand, We use Navarro Frenk White (NFW) profile [2], which is a good fitting function to density profile of cold dark matter in cosmological simulation, as the initial halo density profile. NFW profile reads

$$\rho_{\text{NFW}}(r) = \frac{\rho_0}{\frac{r}{R_s} \left(1 + \frac{r}{R_s}\right)^2} \quad (2.68)$$

, where r_s is the scale radius and ρ_0 is the characteristic density. NFW profile have two parameters, r_s and ρ_0 , which can be transform to halo mass M_h and concentration parameter c defined as

$$c = \frac{R_{\text{vir}}}{R_s} \quad (2.69)$$

where R_{vir} is virial radius. With given halo mass, the number of parameters reduce to one. The initial potential is constructed by pasting soliton profile with NFW profile, i.e.

$$\rho^{(0)}(r) = \Theta(r_e - r)\rho_s(r) + \Theta(r - r_e)\rho_{\text{NFW}}(r) \quad (2.70)$$

, where r_e is the radius where soliton density profile equals to NFW profile. Finally, substitute this initial density profile into equation (2.34), we obtain the initial potential.

We use the time independent perturbation theory to find the self-consistent solution. Firstly, we have zeroth order Hamiltonian $H_0 = -\frac{\hbar^2}{2ma^2}\nabla^2 + m\Phi_{\text{in}}$. we set the first order Hamiltonian be $H = -\frac{\hbar^2}{2ma^2}\nabla^2 + m\Phi_{\text{out}}$, hence the first order Hamiltonian is $H_1 = m(\Phi_{\text{out}} - \Phi_{\text{in}})$. The perturbation theory tells that the first order perturbation in energy is

$$\Delta E_{nl} = \langle nlm | H_1 | nlm \rangle \quad (2.71)$$

where

$$H_0 | nlm \rangle = E_{nl} | nlm \rangle \quad (2.72)$$

, the shift of energy will change the amplitudes because the fermionic King distribution depends on energy.

We also set a criterion of self-consistent solution. Let the function

$$D(\Phi_1, \Phi_2) = \frac{1}{R} \int_0^R \left[\frac{(\Phi_1 - \Phi_2)}{0.5(\Phi_1 + \Phi_2)} \right]^2 dr \quad (2.73)$$

denote the difference between two potentials. If $D(\Phi_{\text{in}}, \Phi_{\text{out}}) < 0.01$ we recognize the solution as self-consistent solution.

2.6 Method of constructing artificial halos

We have created several artificial halo and test their behavior in simulations. The method of constructing artificial halos will be shortly describe in this section. First, solve eigenfunctions and eigenvalues by equation (2.63), either use self-consistent solution or use potential obtain from simulation. Second, amplitudes follow equation (2.66), thus we generate amplitudes as two dimensional Gaussian distribution in the complex plane. Namely, the distribution of amplitudes $a = a_r + ia_i$ of certain energy E is

$$f(a_r, a_i) = \frac{1}{2\pi\sigma^2} \exp\left(-\frac{a_r^2 + a_i^2}{2\sigma^2}\right) \quad (2.74)$$

where

$$\sigma = \sqrt{\frac{1}{2} f_{FK}(E)} \quad (2.75)$$

and f_{FK} is the distribution function of fermionic King model. From equations (2.74) and (2.75), we can easily obtain the ensemble average of amplitudes square

$$\begin{aligned} \langle |a|^2 \rangle &= \int f(a_r, a_i) (a_r^2 + a_i^2) da_r da_i \\ &= \int_0^\infty \frac{1}{2\pi\sigma^2} \exp\left(-\frac{r^2}{2\sigma^2}\right) r^2 2\pi r dr \\ &= 2\sigma^2 \\ &= f_{FK}(E) \end{aligned} \quad (2.76)$$

and

$$\begin{aligned} \langle a_1 a_2^* \rangle &= \int f(a_{1r}, a_{1i}) f(a_{2r}, a_{2i}) (a_{1r} a_{2r} + a_{1i} a_{2i} + i(a_{1i} a_{2r} + a_{2i} a_{1r})) da_{1r} da_{1i} da_{2r} da_{2i} \\ &= 0. \end{aligned} \quad (2.77)$$

The last step is constructing wave function by equation (2.64). Note that we set ground state amplitude in another way. Because we know the core mass already, the amplitude square of ground state is fixed. We only have to give a phase to it.

2.7 Time correlation function

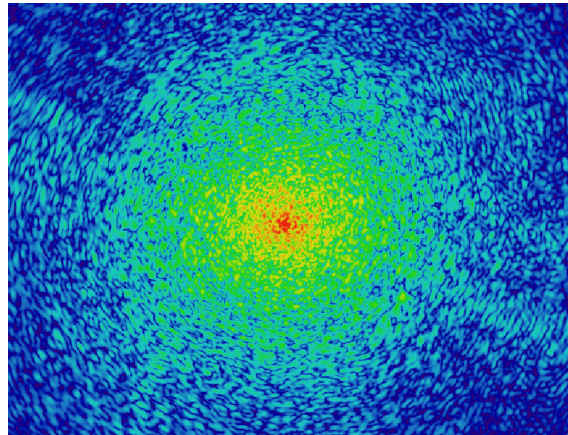
Another important issue we want to consider is the dynamical behavior of granules, therefore we introduce the time correlation function, which is defined as

$$Corr(\tau) = \int_{shell} \delta(\vec{r}, 0) \delta(\vec{r}, \tau) d^3r \quad (2.78)$$

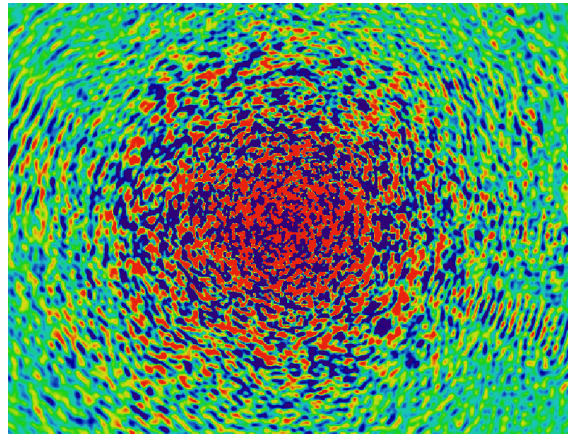
and

$$\delta(\vec{r}, t) = \frac{\rho(\vec{r}, t) - \bar{\rho}(\vec{r}, t)}{\bar{\rho}(\vec{r}, t)}, \quad (2.79)$$

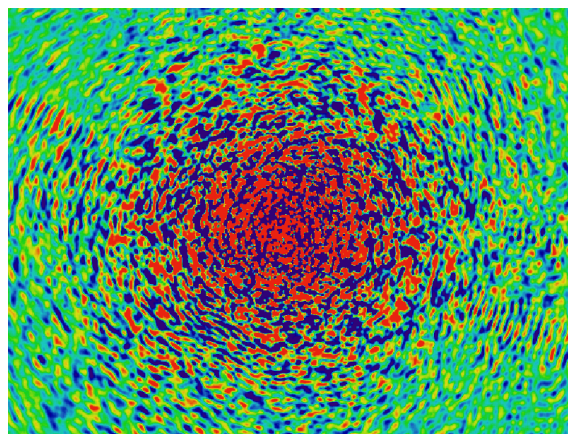
where $\rho(\vec{r}, t)$ is the density. The label shell denote that we only integrate through a thin spherical shell with radius r , and the averaged density $\bar{\rho}$ is also averaged in the thin shell. The reason we average over a thin shell is that if we average the whole volume the inner region will dominate the result. Conceptually, the time correlation function measure the averaged time which the overdensity need to move away from its original position. The results of correlation function for different radius are shown in section 3.4.



(a)



(b)



(c)

Figure 2.1: Density slice of ψ DM halo



Chapter 3

Results

3.1 Probability distribution function

We fit the distribution function by minimizing

$$\chi^2 = \sum_i \left(\frac{DF_i - f(E_i, l_i)}{\sigma_i} \right)^2 \quad (3.1)$$

where

$$\sigma_i = \frac{1}{n_i - 1} \sqrt{\langle y^2 \rangle - \langle y \rangle^2} \quad (3.2)$$

is the standard error, DF_i is the average of amplitudes in the i^{th} bin, E_i and l_i is the energy and angular momentum quantum number of the i^{th} bin, and y is the amplitude square. We analyze five halos and several models, the results are summarized in table 3.1 to 3.5. The reduced χ^2 is defined as

$$\chi_{red} = \frac{\chi^2}{\text{degrees of freedom}} \quad (3.3)$$

Note that we exclude the bins in which there is only one eigenvalue. We also exclude several high energy bins in some cases, because higher energy modes have larger probabilities at large radius, and we expect the region of halos near virial radius may not be in equilibrium yet. Figure 3.1 to figure 3.5 shows the energy distribution function obtain from simulation and the fitting results, different figures show different halos in our simulation. We think it is safe to say that there is no dramatic difference of reduced χ^2 between these models. We also observe ambiguity

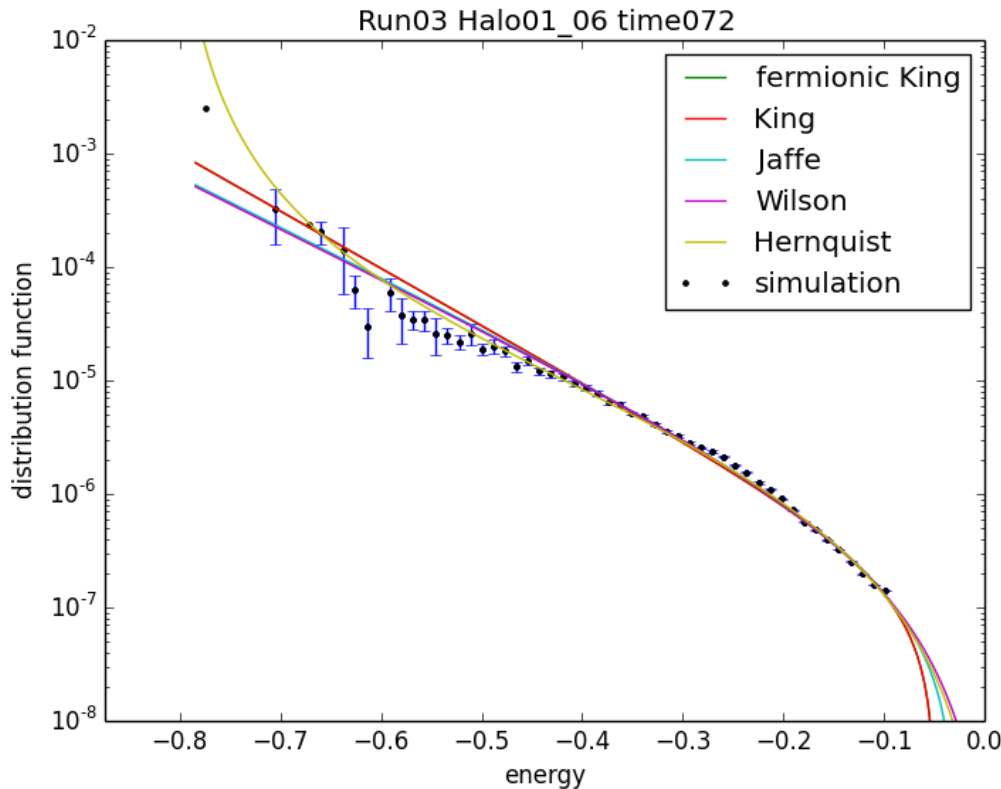


Figure 3.1: Fitting models with energy distribution function, the error bar represent standard error.

when fitting models. We are not sure whether we could obtain global minimum of χ^2 , which need a good guess of initial parameters.

Figure 3.6 to figure 3.5 show the fitting result of Osipkov-Merritt King models. We plot distribution function as two dimensional color map to show the simulation data, model, and residual. We also show the distribution function as function of Q which is defined by equation (2.60). We can see in these figures that for some angular momentum l , the lowest energy eigenvalue become higher when l increase. There is no data in the bottom-right shadow region in figure 3.6a. Due to this limitation, it is hard to tell whether the distribution function of simulation halos depends on angular momentum or not.

Moreover, we test the postulate of random phases for several energy bins. Figure 3.8 shows the amplitudes with $-1.0 < E < -0.95$ in complex plane, every dot represent an amplitude of a eigenstate. It is clear that the simulation halos satisfy

model	χ_{red}^2	bins	degrees of freedom	parameters
King	36.17	60	46	(A, β, E_c)
fermionc King	36.97	60	45	(A, β, E_c, μ)
Jaffe	25.26	60	46	(a, GM, E_c)
Wilson	22.96	60	46	(A, β, E_c)
Hernquist	25.26	60	46	(a, GM, E_c)
Osipkov-Merritt King	4.54	60×99	1400	(A, β, E_c, r_a)
Michie				

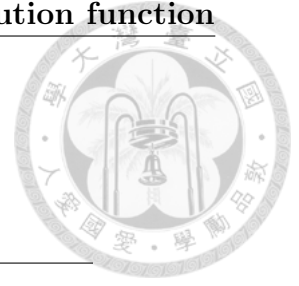
Table 3.1: Run03 Halo01_06 time072

model	χ_{red}^2	bins	degrees of freedom	parameters
King	11.80	50	33	(A, β, E_c)
fermionic King	12.17	50	32	(A, β, E_c, μ)
Jaffe	9.29	50	33	(a, GM, E_c)
Wilson	8.26	50	33	(A, β, E_c)
Hernquist	6.8	50	33	(a, GM, E_c)
Osipkov-Merritt King	64.87	50×40	421	(A, β, E_c, r_a)

Table 3.2: Run03 Halo05 time072

model	χ_{red}^2	bins	degrees of freedom	parameters
King	6.50	70	43	(A, β, E_c)
fermionic King	3.82	70	42	(A, β, E_c, μ)
Jaffe	6.72	70	43	(a, GM, E_c)
Wilson	6.81	70	43	(A, β, E_c)
Hernquist	7.3	70	43	(a, GM, E_c)

Table 3.3: Run03 Halo02_03 time072



model	χ_{red}^2	bins	degrees of freedom	
King	6.62	50	36	(A, β, E_c)
fermionic King	6.80	50	35	(A, β, E_c, μ)
Jaffe	7.08	50	36	(a, GM, E_c)
Wilson	7.42	50	36	(A, β, E_c)
Hernquist	8.48	50	36	(a, GM, E_c)
Osipkov-Merritt King	6.96	50×40	422	

Table 3.4: Run05 Halo01 time072

model	χ_{red}^2	bins	DoF	parameters
King	122.83	60	43	(A, β, E_c)
fermionic King	121.55	60	42	(A, β, E_c, μ)
Jaffe	127.74	60	43	(a, GM, E_c)
Wilson	132.23	60	43	(A, β, E_c)
Hernquist	137.45	60	43	(a, GM, E_c)
Osipkov-Merritt King	6.96	50×40	422	
Michie	33.11	60×94	1147	$(\rho_1, \sigma^2, r_a, E_c)$

Table 3.5: Run05 Halo06 time072

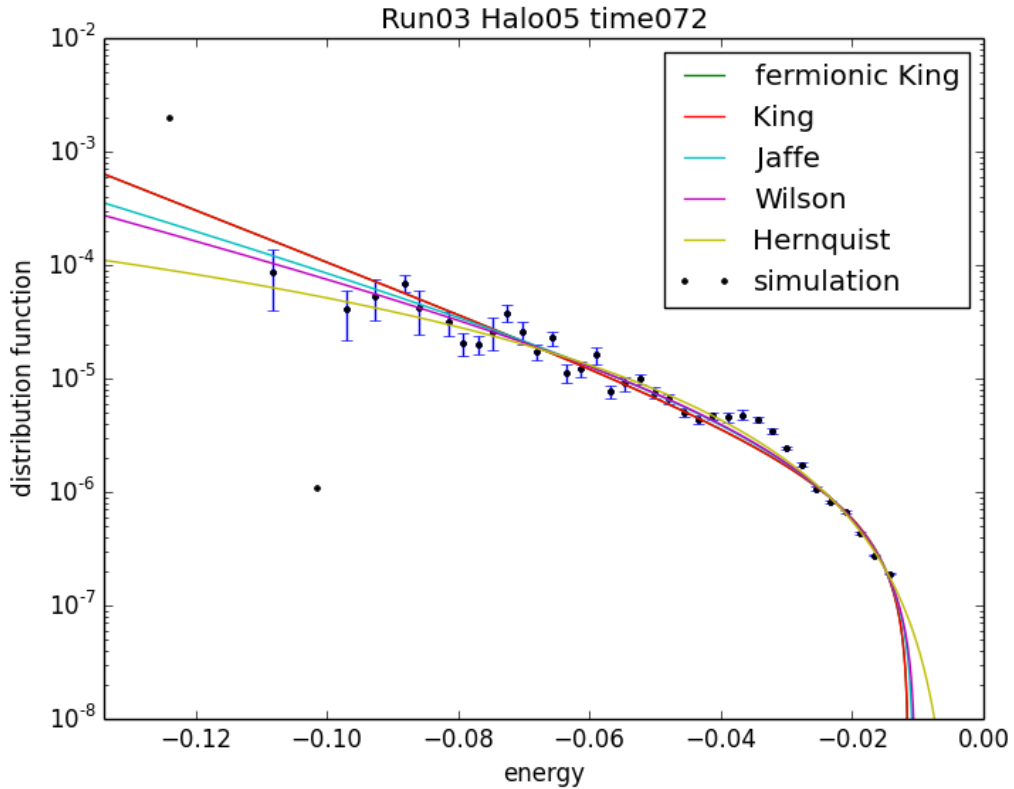


Figure 3.2: Fitting models with energy distribution function

the random phases assumption.

3.2 Self-consistent solution of fermionic King model

In this section we will show several examples of self-consistent solution of potential and density with different parameters, and illustrate the effects of changing the value of them. Also we compare self-consistent solution of density with simulation density, and find a density solution which are very close to the simulation one. It turns out that the parameters of this solution fit the distribution function obtained from simulation fairly well.

We first show a series of self-consistent solution of density and potential with $\mu = -2.5$ but different β , setting escape energy to zero because the upper limit of eigenvalues is $-GM_{vir}m/r_{vir}$, and the exact value of escape energy would not affect much if it is higher than the upper limit. Figure 3.9 to figure 3.14 shows the density

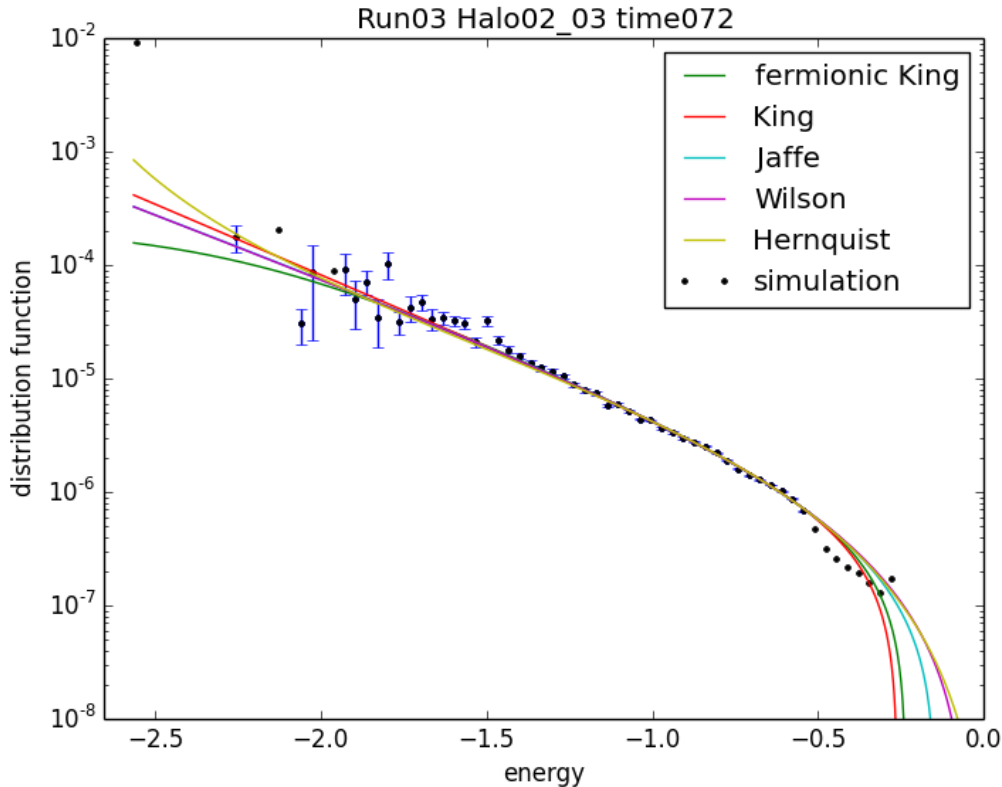


Figure 3.3: Fitting models with energy distribution function, we exclude nine highest bins for this case

profile and potential of self-consistent solution with parameter $\beta = 3.2$ to $\beta = 4.0$. We restrict our discussion to Run03 Halo02_03, which is the most massive halos we could obtain from simulation so far. The mass of this halo is about $7 \times 10^{10} M_{\odot}$, and it does not follow the core-halo relation mentioned in section 2.5. Therefore we make a larger soliton in order to compare simulation with self-consistent solution.

We can see from these figures that when β increase the potential of self-consistent solution becomes shallower. The reason is that we interpret β as inverse temperature, and if temperature is higher the potential should be deeper to satisfy virial condition, which state that potential energy plus two times of kinetic energy is zero for a self-gravity system. On the other hand, figure 3.16 shows density profile and potential of the same $\beta = 3.4$ but different chemical potential μ . We can see that chemical potential reduce the logarithm slope of the most inner part of halos while the density within $r \sim 10^{-3}$ to $r \sim 10^{-3}$ increase because total mass is fixed. As one may

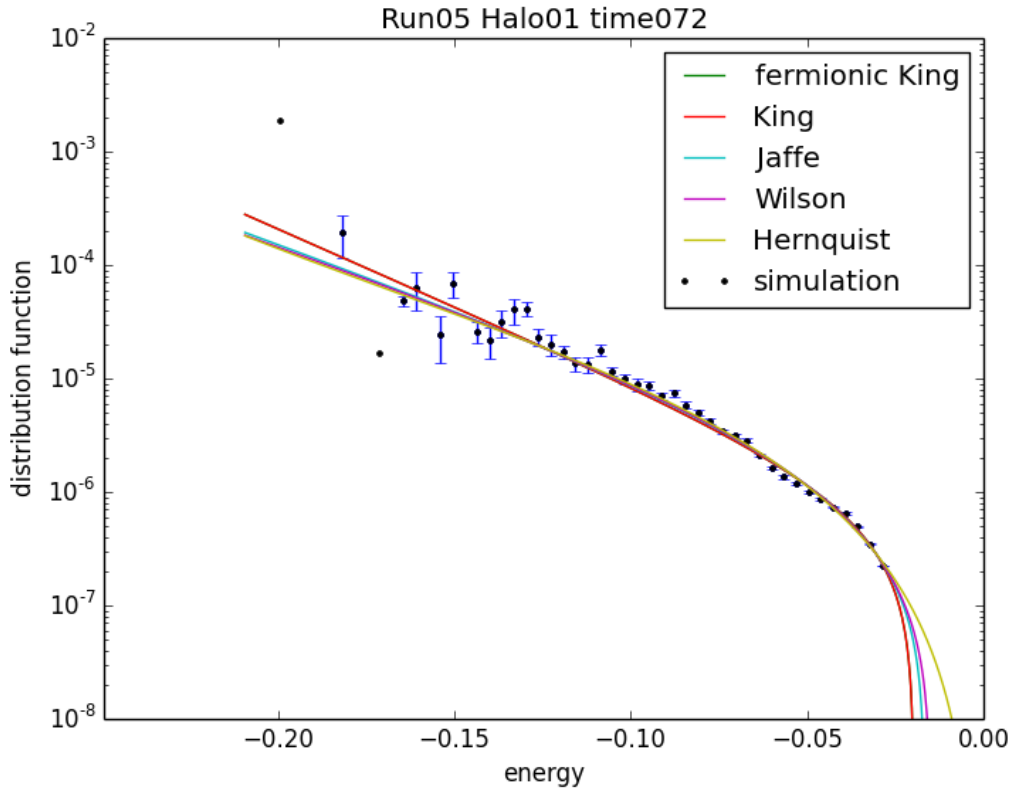


Figure 3.4: Fitting models with energy distribution function, we exclude nine highest bins for this case

expect from distribution function, the existence of chemical potential suppress the amplitudes square of eigenmodes whose energy are below it. These eigenmodes contribute to the inner part of halos thus chemical potential suppress the inner slope of their density profile.

We substitute $\beta = 3.4$ and $\mu = -2.5$ (fig. 3.10) into fermionic King model, calculating the reduced χ^2 using simulation data of distribution function, and find that $\chi_{red}^2 = 5.85$. The result is shown in figure 3.17. On the other hand, we construct a self-consistent solution with parameter obtained by direct fitting, which is $\beta = 3.45550182$ and $\mu = -1.95725734$. Figure 3.18 shows the density and potential for this solution and simulation data. The deviation of this solution from simulation may reflect the fact that we can not precisely obtain the parameters of distribution function because the number of states for lower excited states is too small, which makes large uncertainty about the mean of lower excited states.

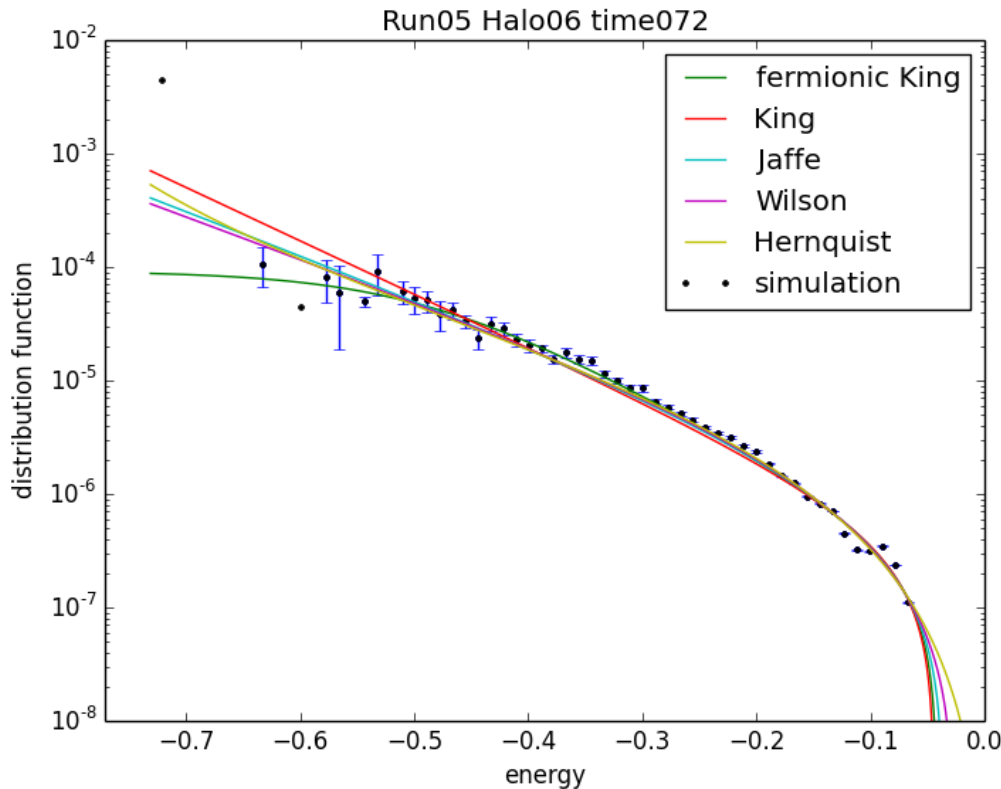


Figure 3.5: Fitting models with energy distribution function. We exclude nine highest bins for this case

3.3 Artificial halos

In this section we show some images of simulation and artificial halos and discuss the stability of artificial halos. We construct three artificial halos using potential obtained by (a) simulation, (b) soliton plus NFW profile, and (c) self-consistent solution with parameters $\beta = 3.4$ and $\mu = -2.5$. Figure 2.1 shows the $z = 0$ slices of density, real part and imaginary part of wave function of simulation halo Run03 Halo02_03. And figure 3.19 shows corresponding slices of artificial halo construct by simulation potential. This potential is calculated form density profile of Run03 Halo02_03, which is the most massive halo we have. Finally, figure 3.20 shows artificial halo using potential of self-consistent solution.

From these figures, we can see that simulation halo is anisotropic in outer region compare with artificial halo, and both of them are isotropic in inner region. This result shows evidence that distribution function should depend on angular momentum

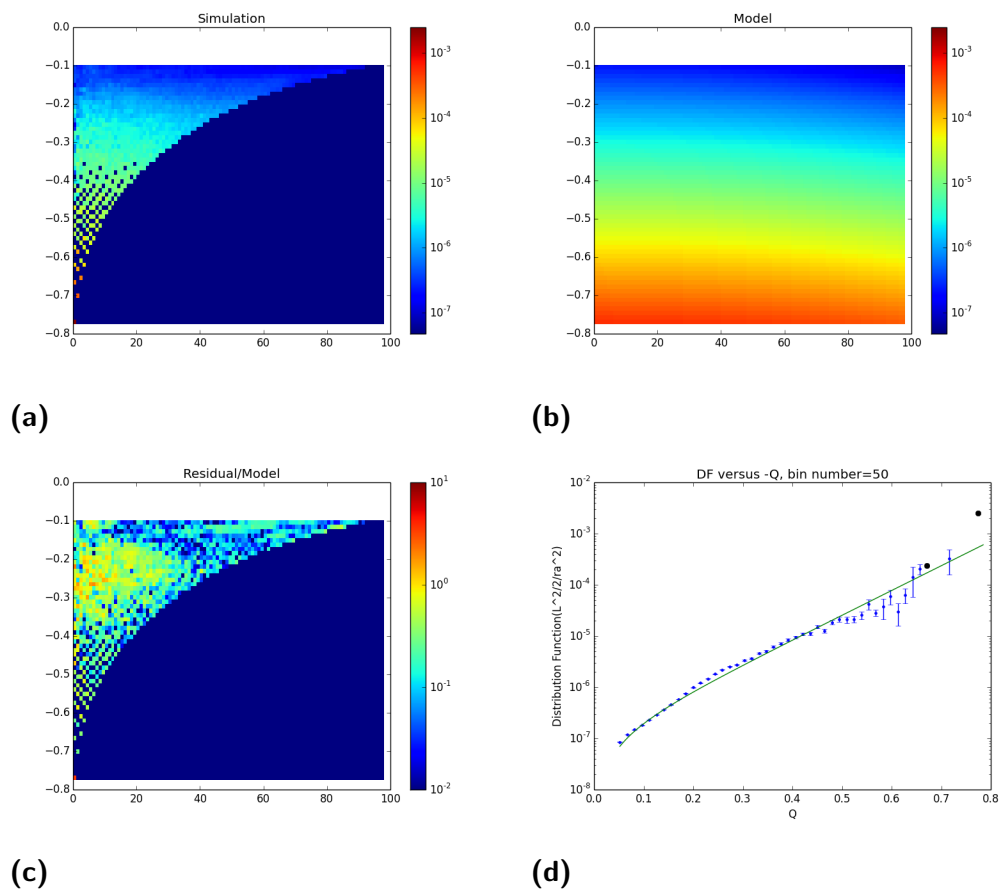


Figure 3.6: OM King model Run03 Halo01_06 time072

or it is not virialized in the outer region, while direct fitting face the challenge that is hard to determine the dependence of angular momentum, which was discussed in section 3.1.

We also shows the evolution of density profile by running simulation for about one free-fall time at virial radius. Figure 3.21 shows the evolution of simulation halo Run03 Halo02_03 and artificial halo made by simulation potential. They evolve roughly the same way, a stable outer halo with an oscillating soliton, while the density of inner part of artificial halo decrease to form a more stable configuration in very short time. This may be caused by the fact that simulation potential and parameters of artificial are not self-consistent. On the other hand, the evolution of artificial halo made by self-consistent solution is shown in figure 3.22(black curve). The whole halo is stable and soliton also oscillate, but with a smaller amplitude compare with simulation halo. We also show the evolution of artificial halo made by

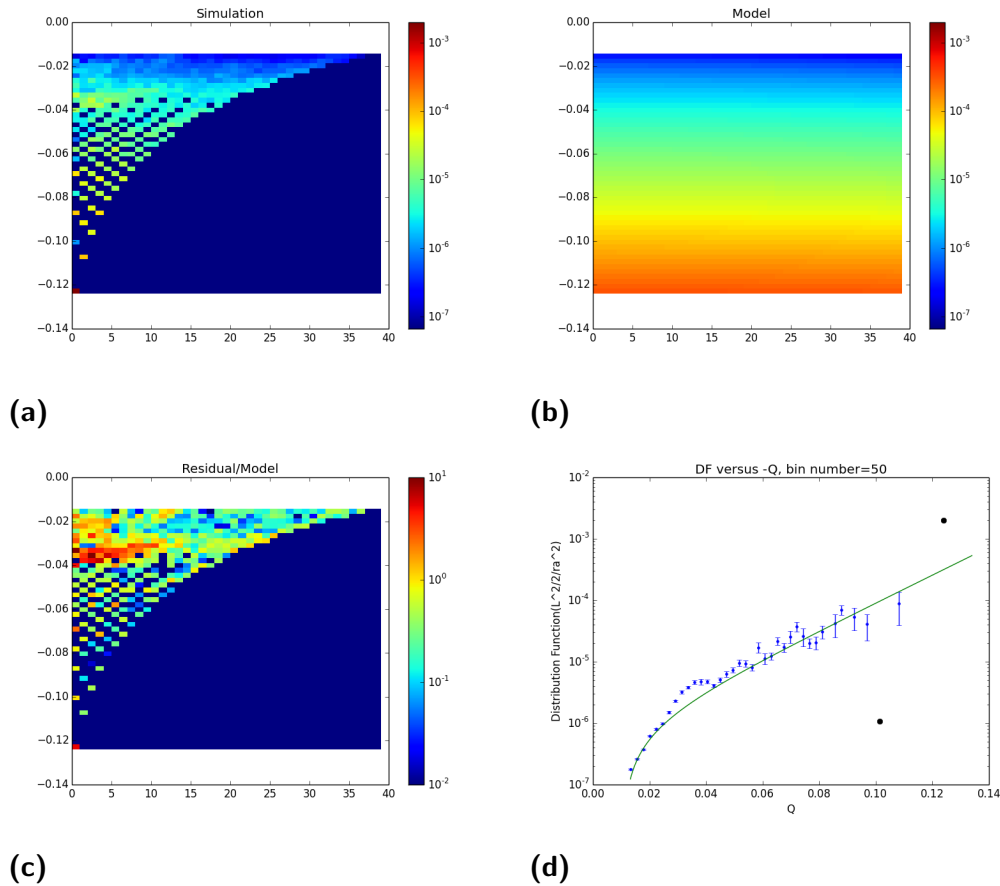
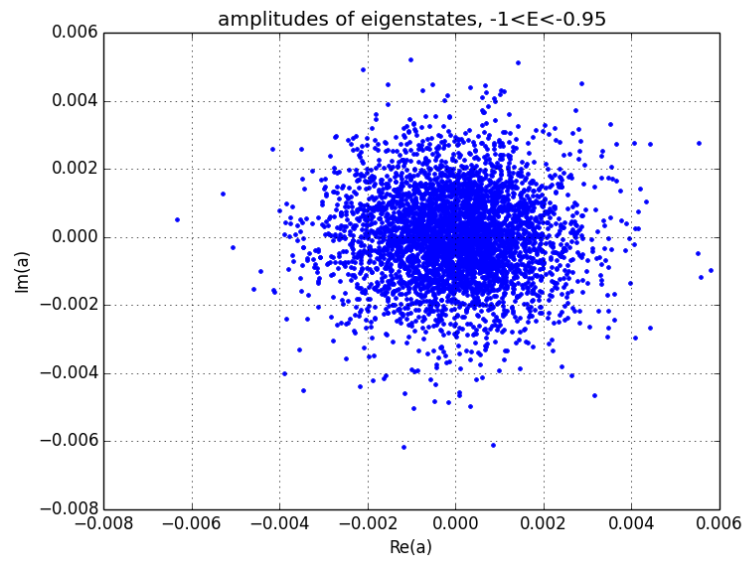


Figure 3.7: OM King model Run03 Halo05 time072

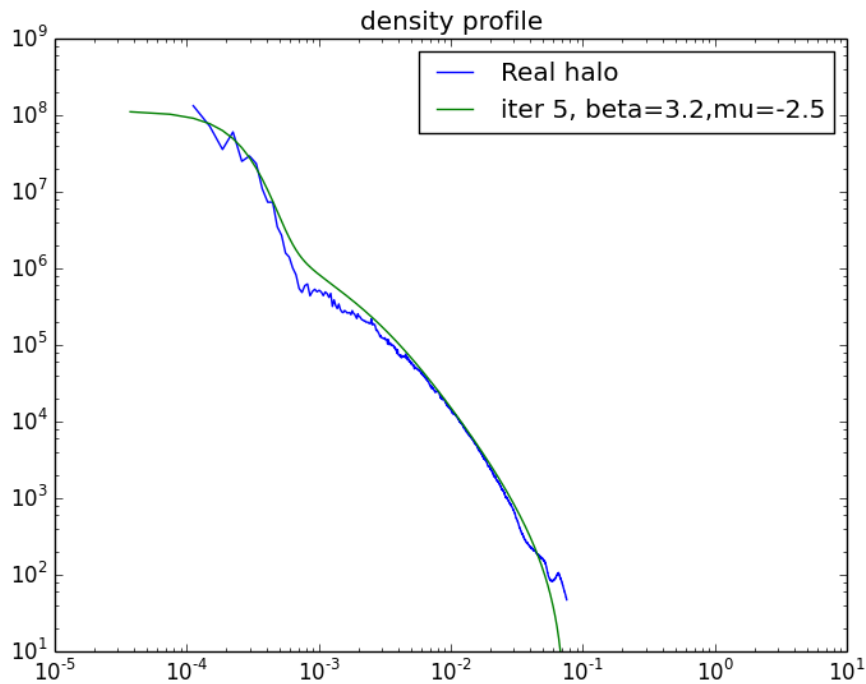
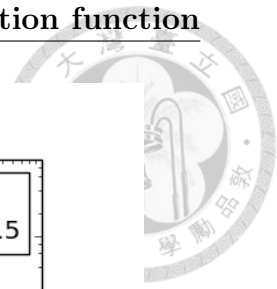
soliton plus NFW potential. It relax into more stable configuration within a free-fall time at virial radius.

3.4 Time correlation function

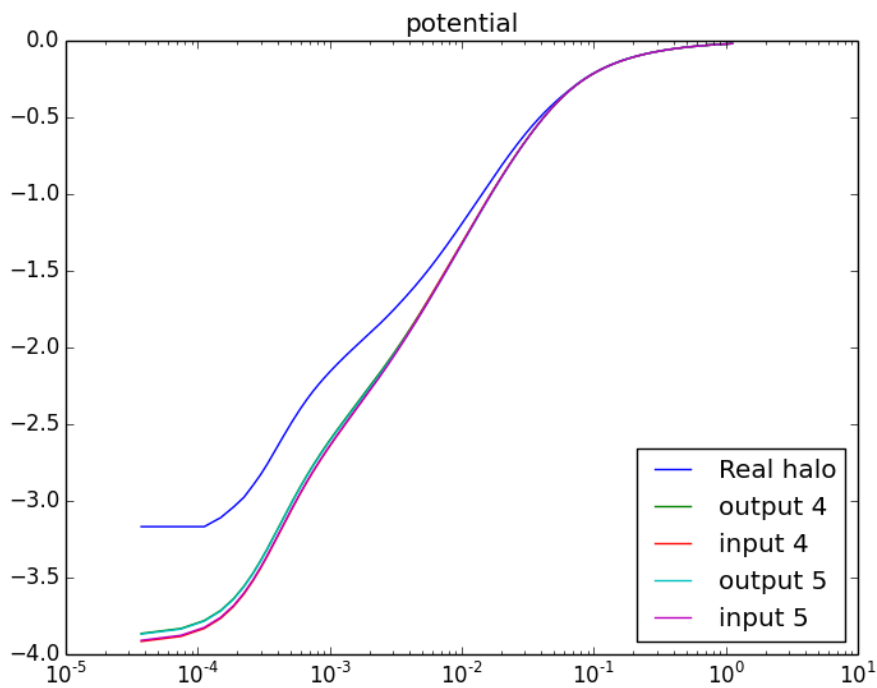
The result of time correlation function defined in section 2.7 are shown in figure 3.23. We use self-consistent solution with $\beta = 3.4$ and $\mu = -2.5$. r_1 to r_9 denote radius of shells in which we calculate correlation function. We take log spacing in this case and the largest radius r_9 is about half of the virial radius. The width of the shells is $\frac{1}{300}$ virial radius, around 3 grids of our simulation box. The unit of time is $1/6$ ground state period. Note that we exclude ground state when we calculate correlation function. We can see from this figure that the inner most radius r_1 have a strong correlation after one hundred steps. As radius increase, the correlation after

**Figure 3.8**

first drop gradually decay. This feature is caused by the fact that lower excited states are dominant at small radius, and there are not enough states to make correlation function drop to zero.

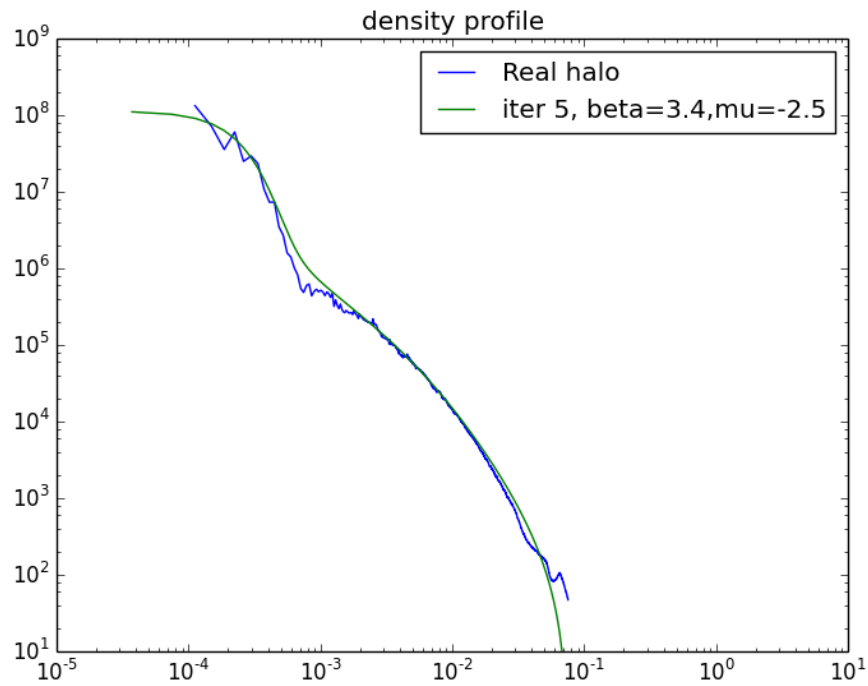


(a)

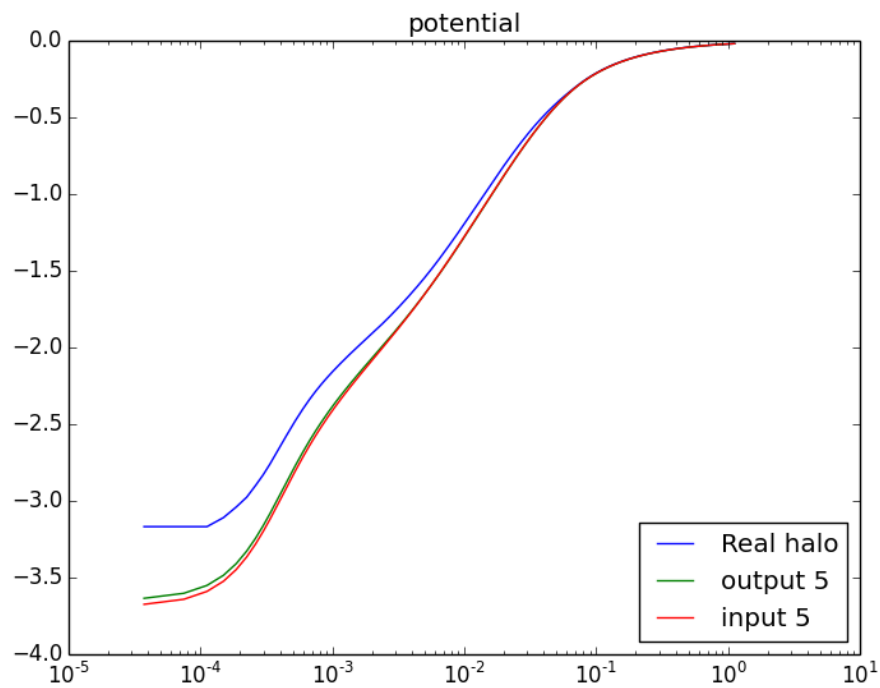


(b)

Figure 3.9: (a) density profile of self-consistent solution (green) and simulation halo (blue). (b) input (red) and output (green) potential of fifth iteration compare with simulation halo (blue)

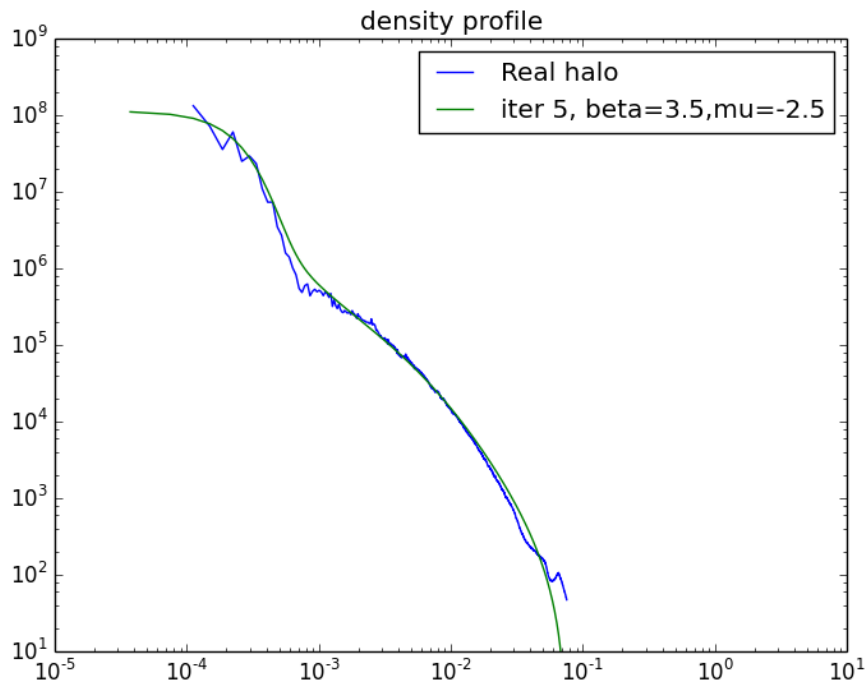
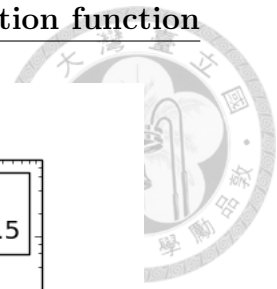


(a)

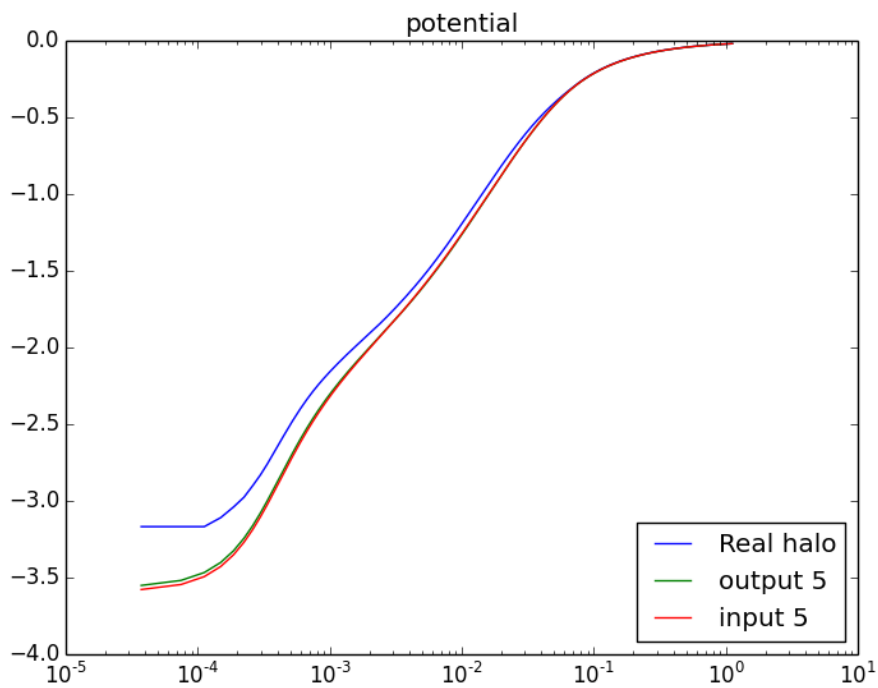


(b)

Figure 3.10: (a) density profile of self-consistent solution (green) and simulation halo (blue). (b) input (red) and output (green) potential of fifth iteration compare with simulation halo (blue)

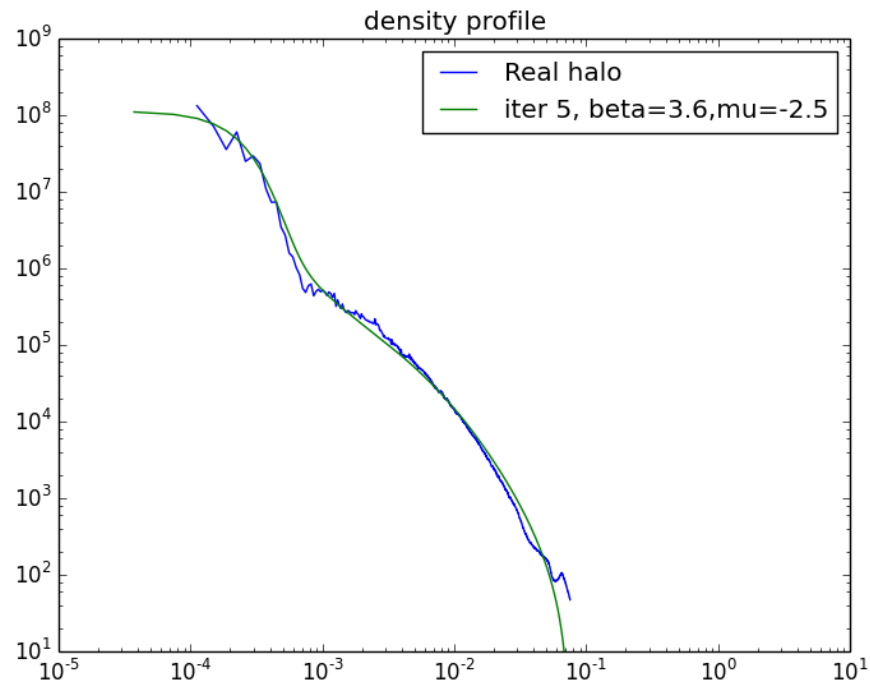


(a)

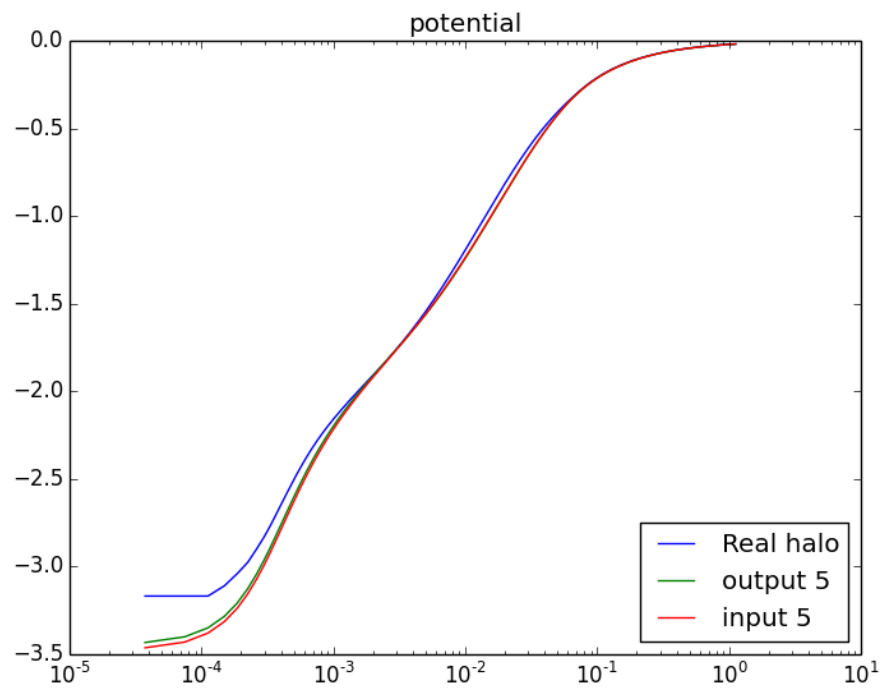


(b)

Figure 3.11: (a) density profile of self-consistent solution (green) and simulation halo (blue). (b) input (red) and output (green) potential of fifth iteration compare with simulation halo (blue)

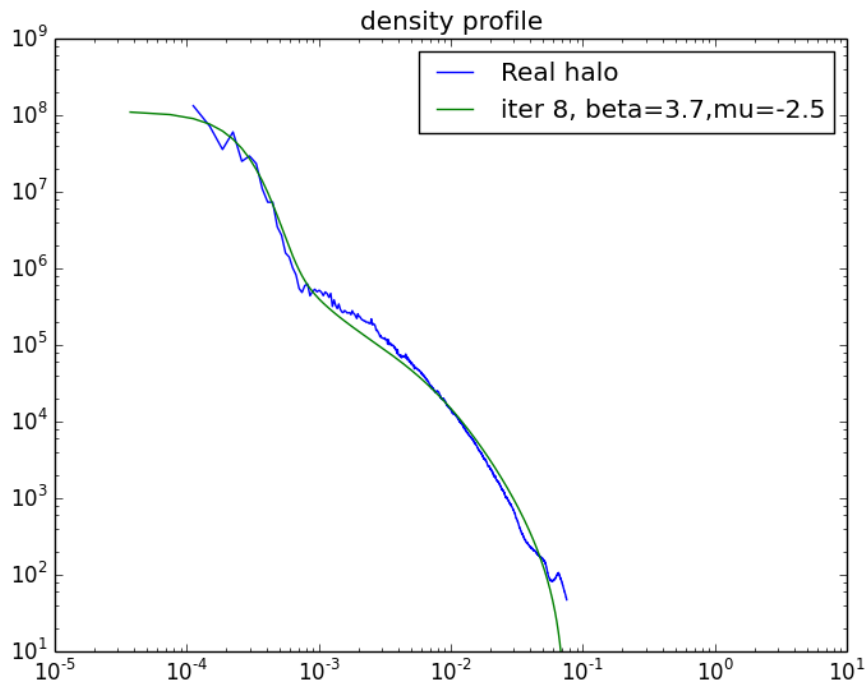
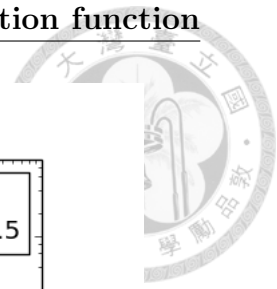


(a)

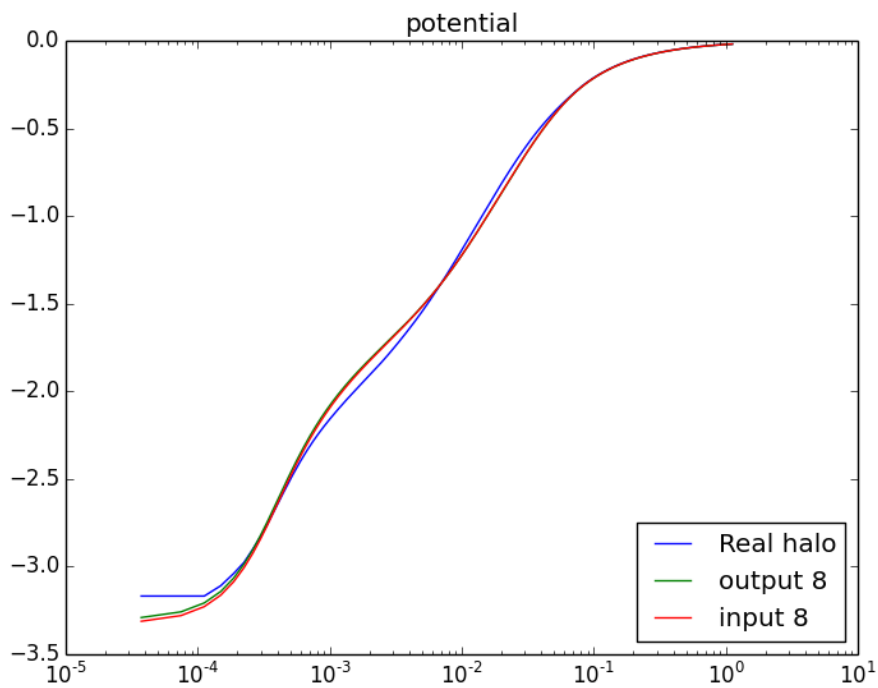


(b)

Figure 3.12: (a) density profile of self-consistent solution (green) and simulation halo (blue). (b) input (red) and output (green) potential of fifth iteration compare with simulation halo (blue)

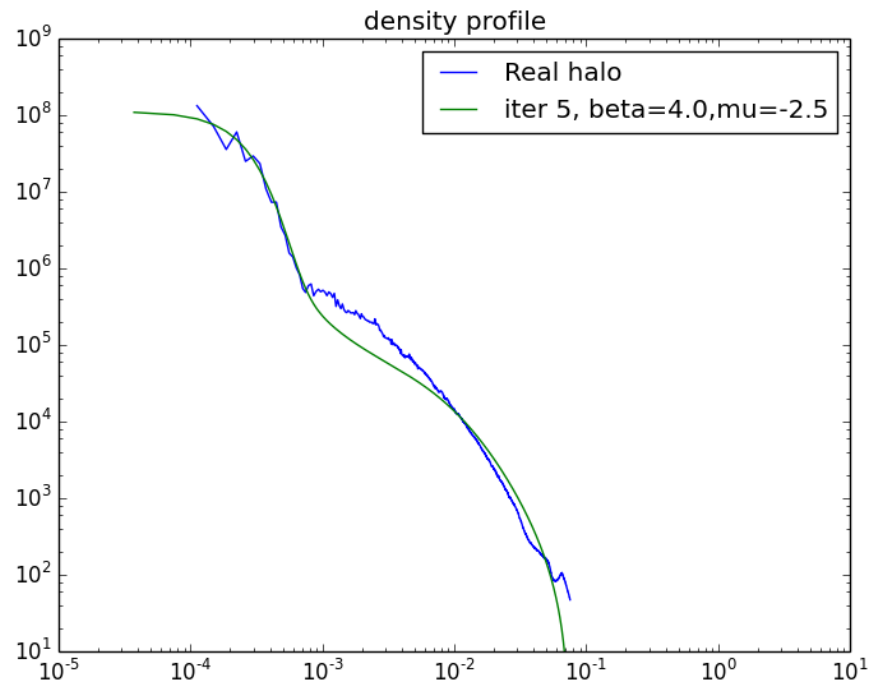


(a)

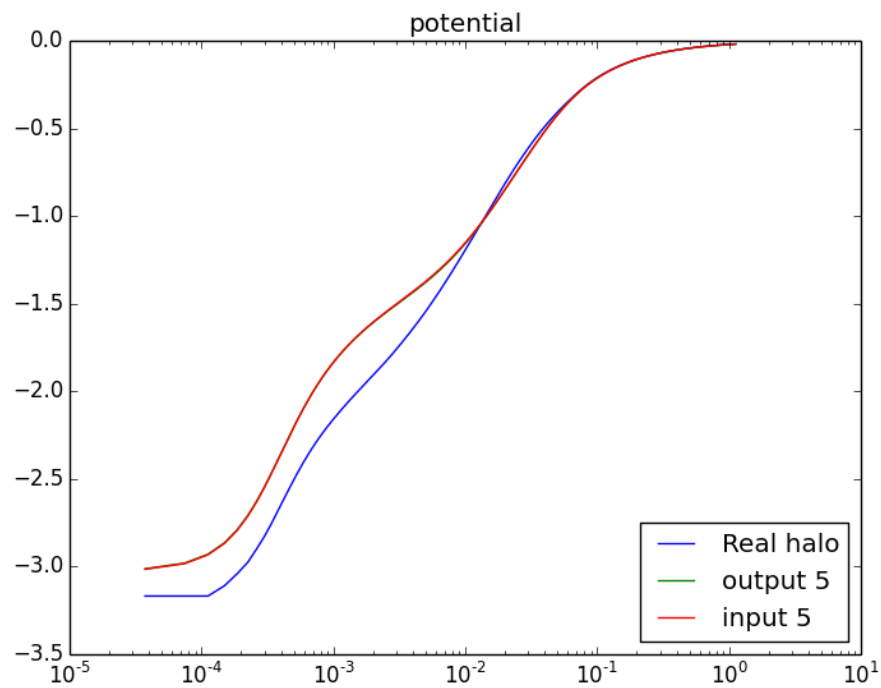


(b)

Figure 3.13: (a) density profile of self-consistent solution (green) and simulation halo (blue). (b) input (red) and output (green) potential of fifth iteration compare with simulation halo (blue)

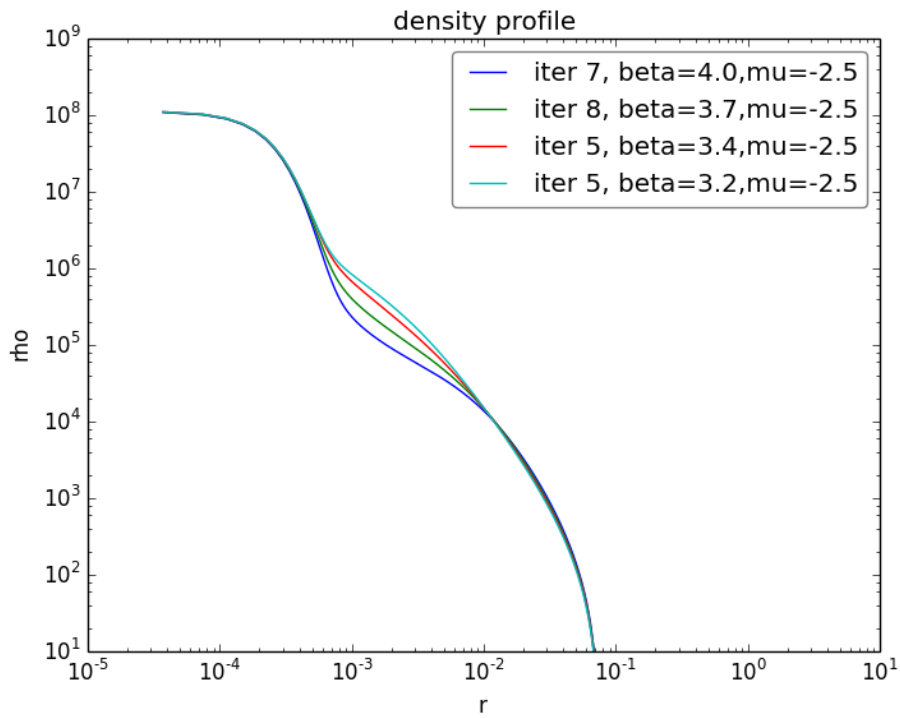


(a)

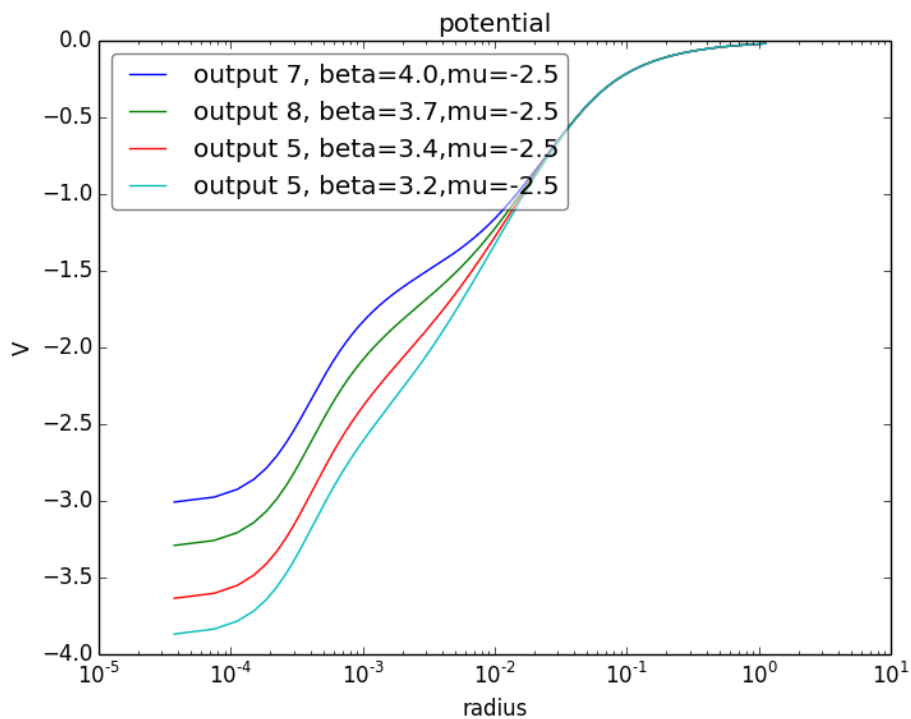


(b)

Figure 3.14: (a) density profile of self-consistent solution (green) and simulation halo (blue). (b) input (red) and output (green) potential of fifth iteration compare with simulation halo (blue)

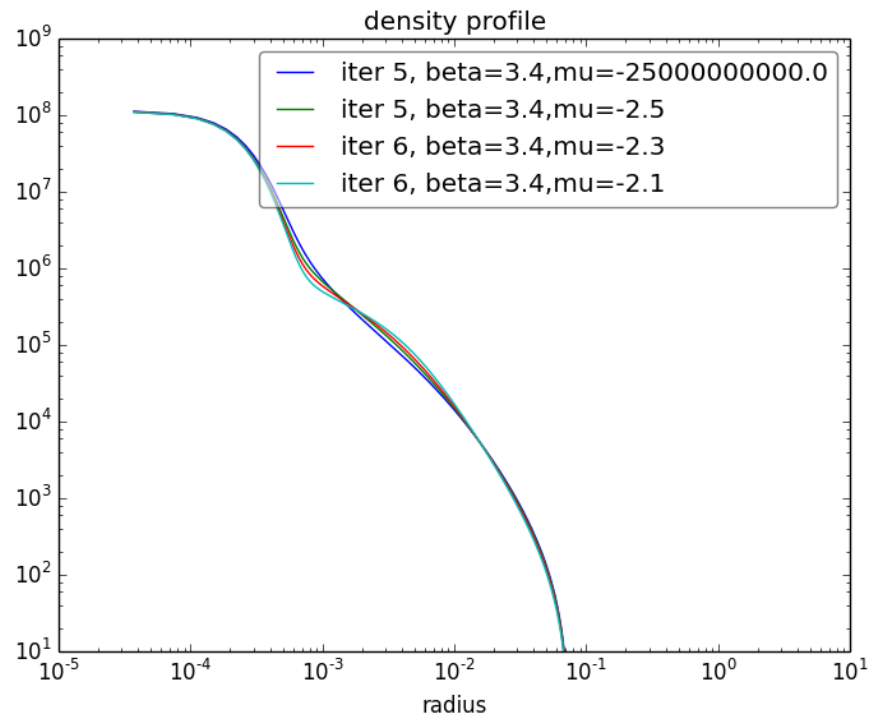


(a)

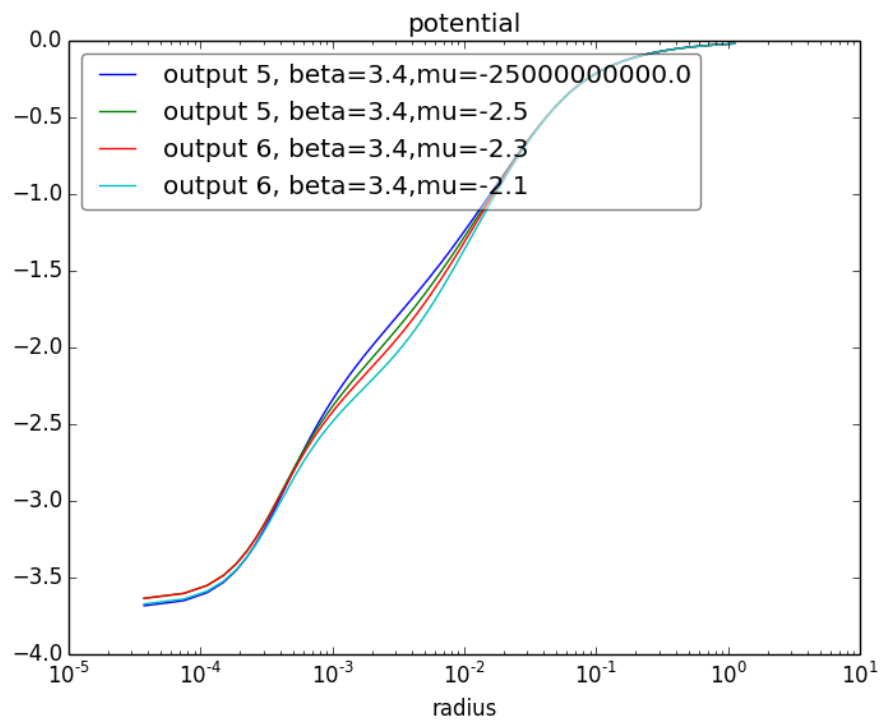


(b)

Figure 3.15: (a) density profile of self-consistent solution with different β .
 (b) output potential of self-consistent solution with different β .



(a)



(b)

Figure 3.16: (a) density profile of self-consistent solution with different μ .
(b) output potential of self-consistent solution with different μ

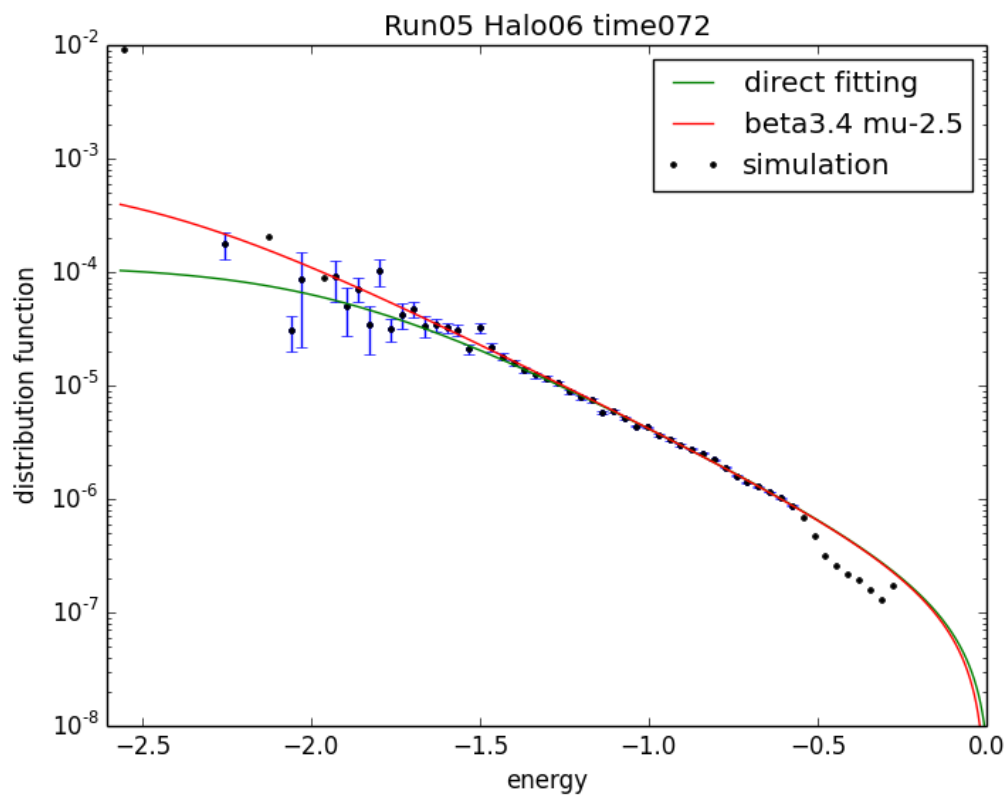
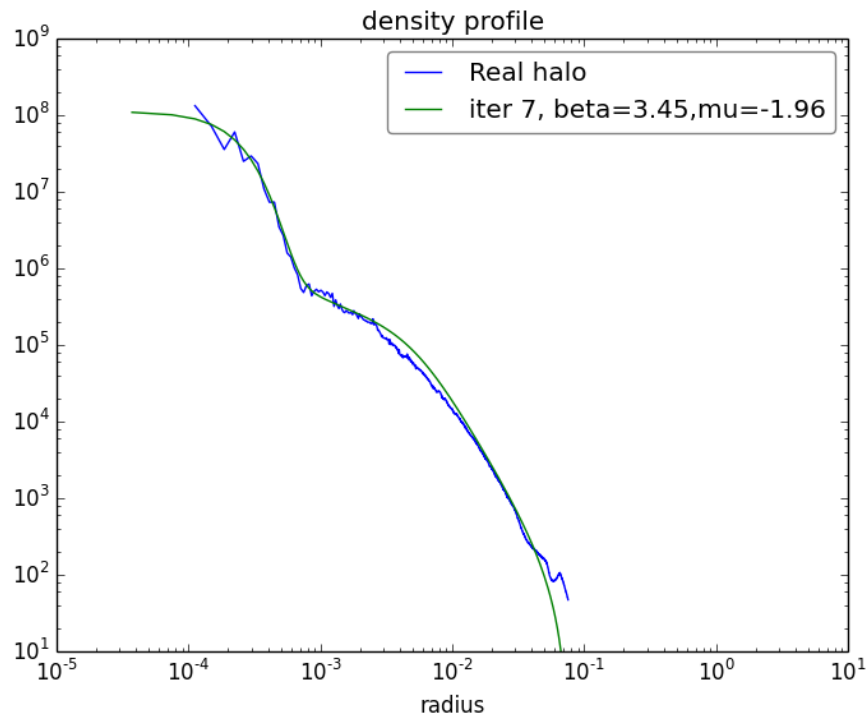
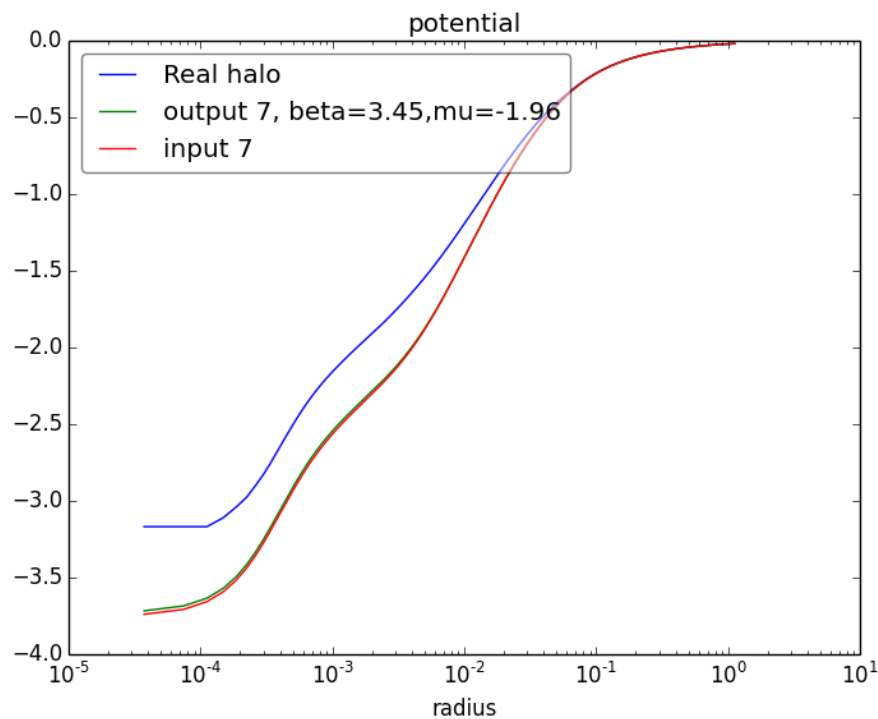


Figure 3.17: Distribution function fitted by $\beta = 3.4$, $\mu = -2.5$, and $E_c = 0$ (red) compare with direct fitting (green).

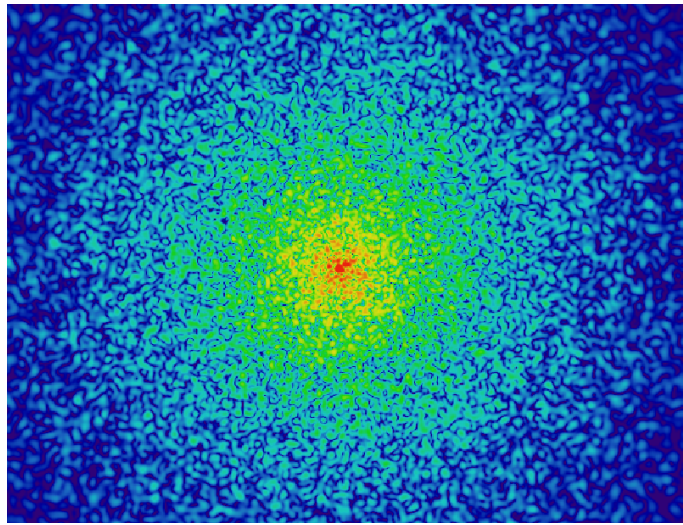


(a)

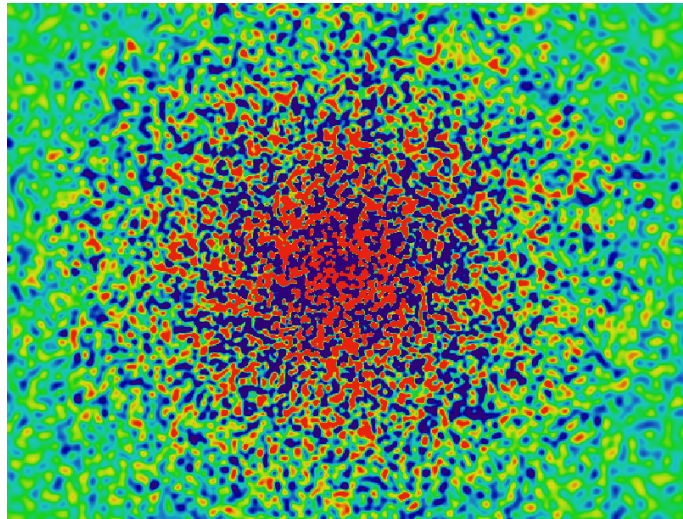


(b)

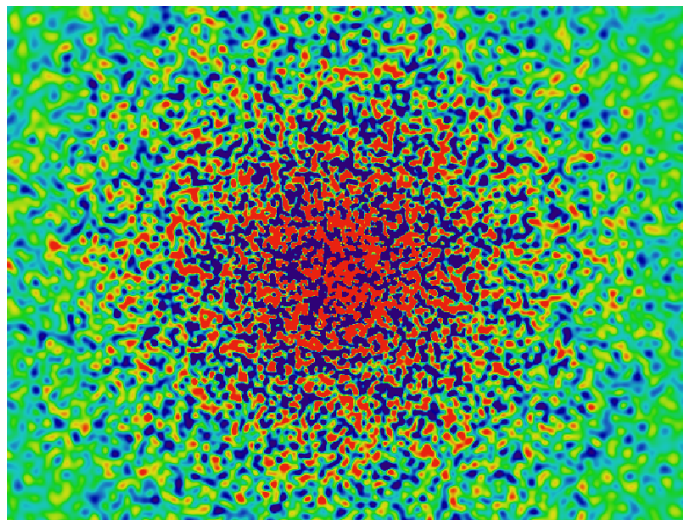
Figure 3.18: Self-consistent solution with parameters obtained from fitting (a) density profile of self-consistent solution (green) and simulation halo (blue). (b) input (red) and output (green) potential of fifth iteration compare with simulation halo (blue).



(a)

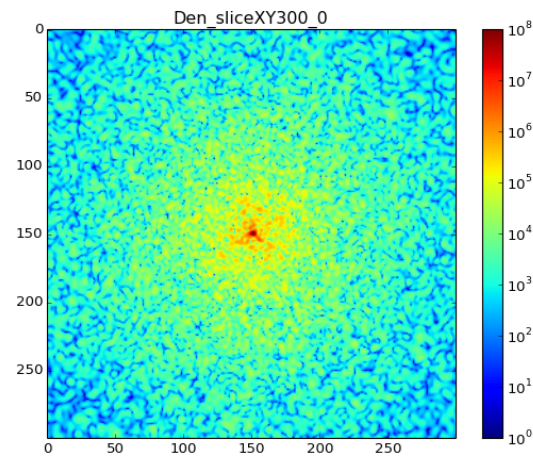


(b)

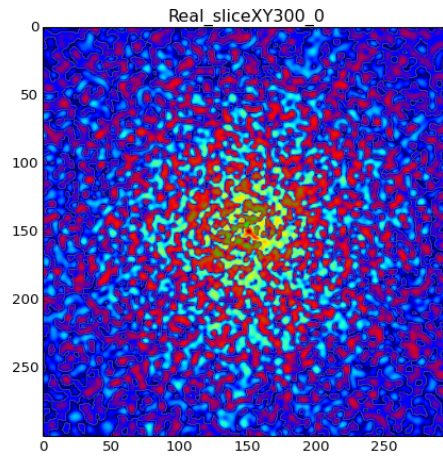


(c)

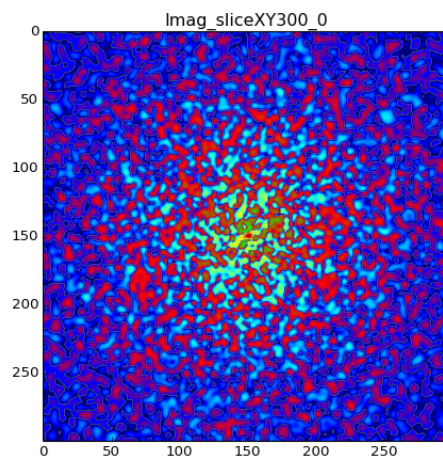
Figure 3.19: Density slice of ψ DM halo



(a)



(b)



(c)

Figure 3.20: Density slice of ψ DM halo

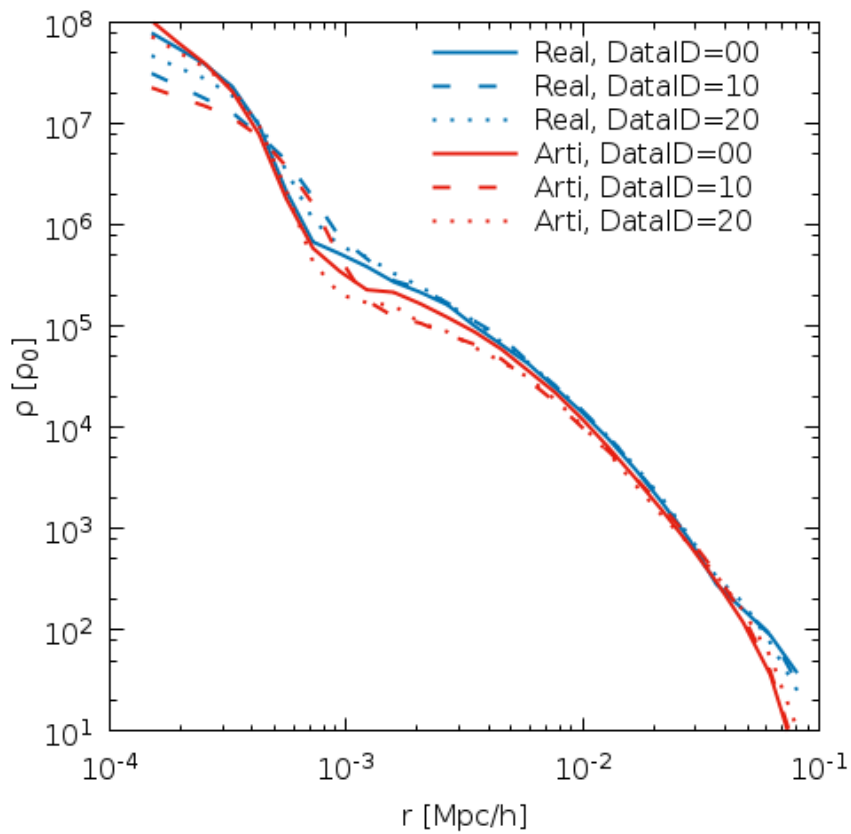
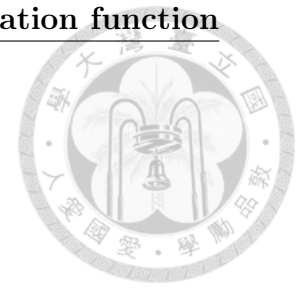


Figure 3.21: Density profile evolves about one free-fall time at virial radius. Here the red curve denote artificial halo construct by simulation potential, and blue curves denote simulation halo. Soliton oscillate in both cases and the outer part of halos are stable as well.

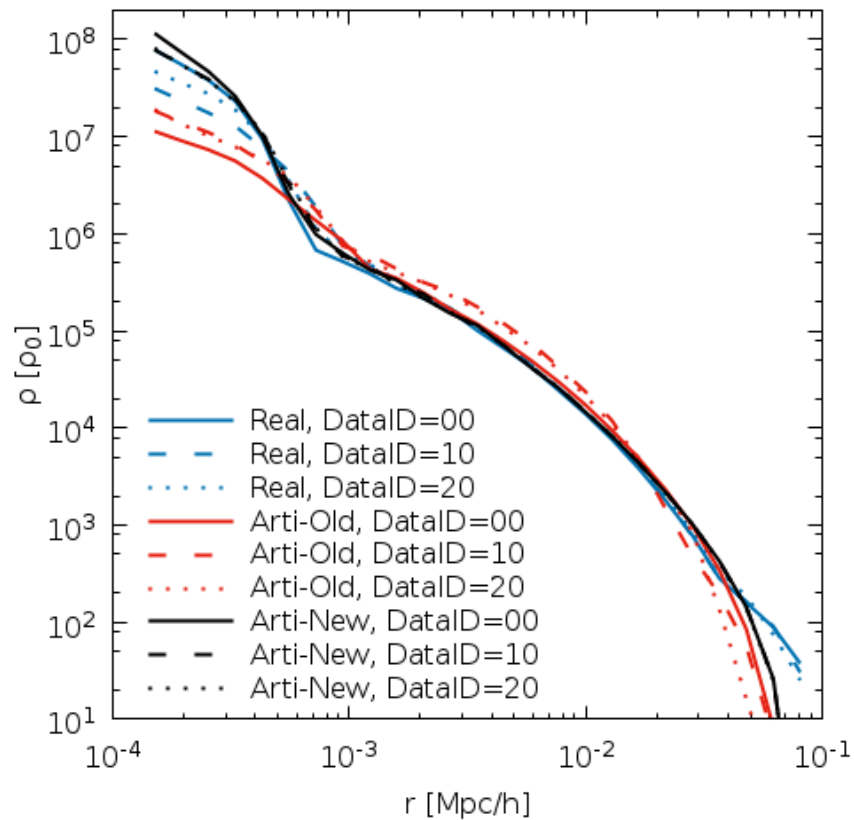


Figure 3.22: Density profile evolves about one free-fall time at virial radius. The Arti-Old denote the artificial halo constructed by soliton plus NFW potential. Arti-New denote artificial halo constructed by self-consistent solution potential with $\beta = 3.4$ and $\mu = -2.5$. The self-consistent solution halo is stable while with soliton oscillate slightly compare to simulation halo. While soliton plus NFW halo need time to relax to a steady state.

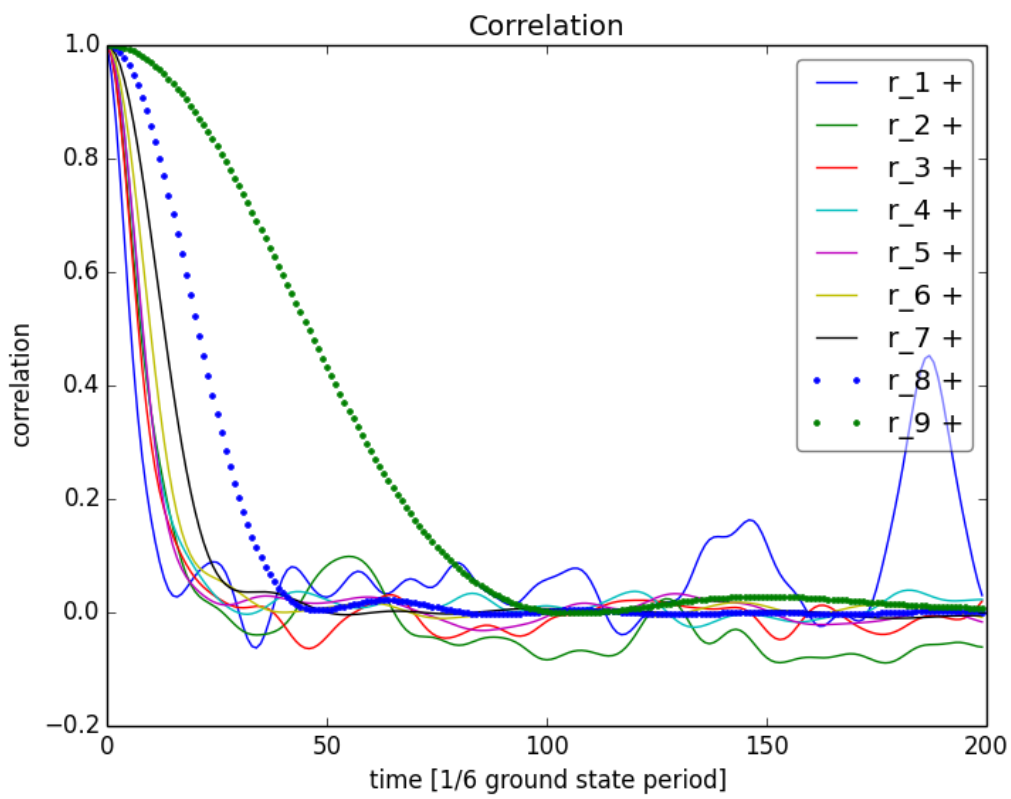


Figure 3.23: Time correlation function of self-consistent solution with $\beta = 3.4$ and $\mu = -2.5$



Chapter 4


Conclusion

To conclude, we have shown that the probability distribution function of a spherically symmetric ψ dark matter halo which obeys Schrödinger-Poisson equation at late time can be describe by several classical distribution function models. Moreover, we show that we can obtain self-consistent solutions of density and potential of ψ DM by utilizing some technics as well as fermionic King model. The artificial halos construct by self-consistent solution is stable and similar with simulation halo for the region whose radius is smaller than one third of virial radius, while fail to represent simulation halo at large radius. We also calculate time correlation function for this halo, and find that the correlation time increase as radius increase.



Bibliography

- [1] James S. Bullock. Notes on the Missing Satellites Problem. *arXiv:1009.4505 [astro-ph]*, September 2010.
- [2] Julio F. Navarro, Carlos S. Frenk, and Simon D. M. White. The Structure of Cold Dark Matter Halos. *The Astrophysical Journal*, 462:563, May 1996.
- [3] B. Moore, F. Governato, T. Quinn, J. Stadel, and G. Lake. Resolving the Structure of Cold Dark Matter Halos. *The Astrophysical Journal Letters*, 499(1):L5, 1998.
- [4] Ben Moore. Evidence against dissipation-less dark matter from observations of galaxy haloes. *Nature*, 370(6491):629–631, August 1994.
- [5] Ricardo A. Flores and Joel R. Primack. Observational and theoretical constraints on singular dark matter halos. *The Astrophysical Journal*, 427:L1, May 1994.
- [6] W. J. G. de Blok and S. S. McGaugh. The dark and visible matter content of low surface brightness disc galaxies. *Monthly Notices of the Royal Astronomical Society*, 290(3):533–552, September 1997.
- [7] N. C. Amorisco, A. Agnello, and N. W. Evans. The core size of the Fornax dwarf spheroidal. *Monthly Notices of the Royal Astronomical Society: Letters*, page sls031, December 2012.
- [8] Anatoly Klypin, Andrey V. Kravtsov, Octavio Valenzuela, and Francisco Prada. Where Are the Missing Galactic Satellites? *The Astrophysical Journal*, 522(1):82, 1999.

- 
- [9] Mario Mateo. Dwarf Galaxies of the Local Group. *Annual Review of Astronomy and Astrophysics*, 36(1):435–506, 1998.
- [10] P. J. E. Peebles. Fluid Dark Matter. *The Astrophysical Journal Letters*, 534(2):L127, 2000.
- [11] Jeremy Goodman. Repulsive dark matter. *New Astronomy*, 5(2):103–107, April 2000.
- [12] Wayne Hu, Rennan Barkana, and Andrei Gruzinov. Fuzzy Cold Dark Matter: The Wave Properties of Ultralight Particles. *Physical Review Letters*, 85(6):1158–1161, August 2000.
- [13] Sang-Jin Sin. Late-time phase transition and the galactic halo as a Bose liquid. *Physical Review D*, 50(6):3650–3654, September 1994.
- [14] Hsi-Yu Schive, Tzihong Chiueh, and Tom Broadhurst. Cosmic structure as the quantum interference of a coherent dark wave. *Nature Physics*, 10(7):496–499, July 2014.
- [15] M. Membrado, A. F. Pacheco, and J. Sañudo. Hartree solutions for the self-Yukawian boson sphere. *Physical Review A*, 39(8):4207–4211, April 1989.
- [16] James Binney and Scott Tremaine. *Galactic Dynamics: (Second Edition)*. Princeton University Press, October 2011.
- [17] Pierre-Henri Chavanis. On the ‘coarse-grained’ evolution of collisionless stellar systems. *Monthly Notices of the Royal Astronomical Society*, 300(4):981–991, November 1998.
- [18] Edward Seidel and Wai-Mo Suen. Dynamical evolution of boson stars: Perturbing the ground state. *Physical Review D*, 42(2):384–403, July 1990.
- [19] Abril Suárez and Pierre-Henri Chavanis. Hydrodynamic representation of the Klein-Gordon-Einstein equations in the weak field limit. *Journal of Physics: Conference Series*, 654(1):012008, 2015.

- [20] Anthony Zee. *Quantum field theory in a nutshell*. Princeton university press, 2010.
- [21] E Anderson, Z Bai, C Bischof, S Blackford, J Demmel, J Dongarra, J Du Croz, A Greenbaum, S Hammarling, A McKenney, and D Sorensen. *{LAPACK} Users' Guide*. Society for Industrial and Applied Mathematics, 1999.
- [22] V. Ledoux. Study of special algorithms for solving Sturm-Liouville and Schrodinger equations. *ResearchGate*, January 2007.
- [23] Lars Hernquist. An analytical model for spherical galaxies and bulges. *The Astrophysical Journal*, 356:359–364, June 1990.
- [24] Walter Jaffe. A simple model for the distribution of light in spherical galaxies. *Monthly Notices of the Royal Astronomical Society*, 202(4):995–999, January 1983.
- [25] C. P. Wilson. Dynamical models of elliptical galaxies. *The Astronomical Journal*, 80:175–187, March 1975.
- [26] Ivan R. King. The structure of star clusters. III. Some simple dynamical models. *The Astronomical Journal*, 71:64, February 1966.
- [27] R. W. Michie. On the distribution of high energy stars in spherical stellar systems. *Monthly Notices of the Royal Astronomical Society*, 125:127, 1963.
- [28] R. Ruffini and L. Stella. On semi-degenerate equilibrium configurations of a collisionless self-gravitating Fermi gas. *Astronomy and Astrophysics*, 119:35–41, March 1983.
- [29] D. Lynden-Bell. Statistical mechanics of violent relaxation in stellar systems. *Monthly Notices of the Royal Astronomical Society*, 136:101, 1967.
- [30] Hsi-Yu Schive, Ming-Hsuan Liao, Tak-Pong Woo, Shing-Kwong Wong, Tzihong Chiueh, Tom Broadhurst, and W-Y. Pauchy Hwang. Understanding the Core-Halo Relation of Quantum Wave Dark Matter from 3D Simulations. *Physical Review Letters*, 113(26):261302, December 2014.